Diurnal Cycle of the ITCZ in DYNAMO

PAUL E. CIESIELSKI, RICHARD H. JOHNSON, AND WAYNE H. SCHUBERT

Department of Atmospheric Science, Colorado State University, Fort Collins, Colorado

JAMES H. RUPPERT JR.

Max Planck Institute for Meteorology, Hamburg, Germany

ABSTRACT

During the 2011 special observing period of the Dynamics of the Madden–Julian Oscillation (DYNAMO) field experiment, two sounding arrays were established over the central Indian Ocean, one north and one south of the equator, referred to here as the NSA and SSA, respectively. Three-hourly soundings from these arrays augmented by observations of radiation and rainfall are used to investigate the diurnal cycle of ITCZ convection during the MJO suppressed phase. During the first half of October, when convection was suppressed over the NSA but prominent over the SSA, the circulation over the sounding arrays could be characterized as a local Hadley cell. Strong rising motion was present within the ITCZ extending across the SSA with compensating subsidence over the NSA. A prominent diurnal pulsing of this cell was observed, impacting conditions on both sides of the equator, with the cell running strongest in the early morning hours (0500–0800 LT) and notably weakening later in the day (1700–2000 LT). The declining daytime subsidence over the NSA may have assisted the moistening of the low to midtroposphere there during the pre-onset stage of the MJO. Apparent heating Q_1 within the ITCZ exhibited a diurnal evolution from early morning bottom-heavy profiles to weaker daytime top-heavy profiles, indicating a progression from convective to stratiform precipitation. Making use of the weak temperature gradient approximation, results suggest that both horizontal radiative heating gradients and direct cloud radiative forcing have an important influence on diurnal variations of vertical motion and convection within the ITCZ.

1. Introduction

The diurnal cycle is a fundamental mode of the circulation and precipitation variability in the tropics. While its characteristics and governing mechanisms over land and coastal regions have been extensively studied and are well understood, the same cannot be said for over the open ocean, where the paucity of observations has limited our ability to fully describe and understand it. Making creative use of surface observations (e.g., COADS, buoy, and scatterometer winds), several studies have examined its structure over the tropical oceans on seasonal to annual time scales (e.g., Deser and Smith 1998; Dai and Deser 1999; Gille et al. 2003). A consistent pattern has emerged from these studies, in which surface divergence in regions of large-scale

subsidence is a maximum (minimum) in the morning (evening) hours. This diurnally varying circulation is compatible with an early morning rainfall maximum in adjacent regions of deep convection and associated overturning circulation in response to cloud-radiative feedbacks (Gray and Jacobson 1977, hereafter GJ77; Randall et al. 1991). Yet, because of a lack of in situ observations, very few studies have examined the modulation of large-scale overturning circulation by diurnally varying organized deep convection. This study addresses this gap.

Nicholls (2015) gives a detailed review of the three main proposed mechanisms by which radiation affects organized oceanic convective systems. The ''convergence/differential radiation'' mechanism was originally proposed by GJ77, based on their observation that rainfall in oceanic deep tropical convection is 2–3 times heavier in the early morning hours than in the late afternoon and evening. This mechanism operates as

Corresponding author: Paul E. Ciesielski, paulc@atmos.colostate.edu

TABLE 1. Summary of studies that used tropical/subtropical field program sounding datasets to examine the diurnal cycle of diagnosed atmospheric fields over the ocean. The last two columns list various attributes of the vertical motion field (e.g., its mean and diurnal amplitude defined here as the peak to peak difference, the vertical location of peak amplitude and diurnal variation, and the LT of peak anomalous subsidence). Note that for TOGA COARE the diurnal characteristics listed here are for convectively disturbed periods.

Field program/study	Location and weather regime	Study duration	Sounding frequency	Mean vertical motion	Vertical motion diurnal cycle
Barbados Oceanographic and Meteorological Experiment (BOMEX; Nitta and Esbensen 1974)	Western Atlantic trade wind	9 days in Jul 1969	1.5 h	$+2\,\mathrm{hPa\,h^{-1}}$ near 800 hPa	$\sim 2\,\mathrm{hPa\,h^{-1}}$ at 0800 LT
GARP Atlantic Tropical Experiment (GATE; Albright et al. 1981)	Eastern Atlantic ITCZ/easterly waves	Three 20-day periods in Jul to Sep 1974	6 h	$-0.7\,\mathrm{hPa\,h^{-1}}$ near 750 hPa	$\sim 1.0\,\mathrm{hPa\,h^{-1}}$ at 0000 LT
Atlantic Stratocumulus Transition Experiment (ASTEX; Ciesielski et al. 2001)	Eastern Atlantic stratoculumus transition zone	14 days in Jun 1992	3 h	$+2.5\,\mathrm{hPa\,h^{-1}}$ near 825 hPa	$\sim 0.8\,\mathrm{hPa\,h^{-1}}$ at 2200 LT
Tropical Ocean and Global Atmosphere Coupled Ocean–Atmosphere Response Experiment (TOGA COARE; Sui et al. 1997)	Western Pacific warm pool	97 days within Nov 1992 to Feb 1993	6 h	$-2\,\mathrm{hPa\,h^{-1}}$ near 400 hPa	$\sim 1.0\,\mathrm{hPa\,h^{-1}}$ at 2200 LT

follows: at night radiative cooling is strong in the clear environment adjacent to regions of disturbed weather, where smaller net cooling occurs. This results in enhanced subsidence in the clear region and low-level convergence into convective regions, and during the day, differential heating between clear and cloudy areas is reduced, leading to weaker convection. A second mechanism, based on the modeling work of Dudhia (1989) and Tao et al. (1996), emphasizes the role of large-scale radiative cooling in increasing rainfall by raising the environmental relative humidity. The third mechanism is referred to as "direct radiative–convective interaction," or simply, the lapse-rate mechanism (Kraus 1963; Randall et al. 1991; Xu and Randall 1995). According to this mechanism, the absorption of shortwave radiation preferentially near cloud top stabilizes the column, in turn suppressing convection during the daytime, while longwave cooling from cloud tops acting alone at night leads to increased lapse rates and rainfall.

Several past studies have explored the diurnal cycle of vertical motion and convection over the open oceans using field campaign upper-air datasets. These studies, spanning a broad spectrum of geographical locations and convective regimes, are briefly summarized in Table 1.[1] The diurnal characteristics of the diagnosed fields vary greatly among the various regions. For example, within the western Atlantic trade-wind regime, Nitta and Esbensen (1974) found that during an undisturbed period in BOMEX, the subsidence field, which peaked near the trade-wind inversion top ($\sim 800\,\mathrm{hPa}$), had a

diurnal amplitude of $\sim 2\,\mathrm{hPa\,h^{-1}}$ with a subsidence maximum (minimum) at 0800 LT (2000 LT). A smaller diurnal amplitude ($\sim 0.8\,\mathrm{hPa\,h^{-1}}$) was observed in the stratocumulus transition zone of ASTEX with peak subsidence at 2200 LT being nearly out of phase with that found in BOMEX (Ciesielski et al. 2001). On the other hand, the deep convective environment of GATE showed an afternoon convective maximum (Albright et al. 1981), while in TOGA COARE the diurnal peak in convection varied depending on the convective regime (Chen and Houze 1997; Sui et al. 1997), with an afternoon peak in suppressed conditions and a late night to early morning peak in disturbed periods. Collectively, these studies reveal a spatial complexity to the diurnal cycle and suggest a variety of processes that influence it.

Observational studies of intertropical convergence zone (ITCZ) convection over the oceans have generally used satellite data and reanalysis products to characterize its behavior. For example, Waliser and Gautier (1993) used two decades of global infrared and visible satellite products to document the seasonal, annual, and interannual variability of the ITCZ. Using 23 years of European Centre for Medium-Range Weather Forecasts (ECMWF) reanalyses, Magnusdottir and Wang (2008) examined the synoptic-scale variability of vorticity within several ITCZ regions and found that their composite structure over the eastern and central Pacific builds westward and tilts cyclonically in the latitudinal direction with time. Employing a statistical method that objectively diagnoses regions of organized ITCZ convection over the eastern Pacific using 3-h satellite data, Bain et al. (2010, 2011) found a diurnal pulsing in

---

[1] Experiment acronyms are listed in the Table 1.

the extent of the ITCZ cloud envelope with a 15% afternoon increase along with a 1300–1600 LT minimum in IR temperatures. The results presented in the current paper are intended to complement these earlier studies by offering a unique perspective on the diurnal cycle of the ITCZ through use of 3-hourly in situ sounding observations.

To investigate the mechanisms responsible for the initiation of the Madden–Julian oscillation (MJO; Madden and Julian 1972) over the Indian Ocean (IO), the Dynamics of the MJO (DYNAMO) experiment was conducted during the period from October 2011 to March 2012 (Yoneyama et al. 2013; Zhang et al. 2013; Zhang 2013). One of the unexpected findings from DYNAMO was that ITCZ convection was present over the Southern Hemisphere IO during the pre-onset (or suppressed) stage leading up to both the October and November MJO events, and then shifted northward to the equator during the MJO convectively active phases (Johnson and Ciesielski 2013; Yoneyama et al. 2013; Kerns and Chen 2014). Later studies have shown that ITCZ convection in the IO region is quite common. Using TRMM rainfall products over the 16-yr period from 1998 to 2013, Sodowsky (2016) and Zhang and Sodowsky (2016) identified 205 ITCZ events lasting 2 days or longer over the IO region (60°–90°E) and 99 MJOs. These studies showed that the majority of these MJOs (~55%) initiated within 2 weeks of a preceding IO ITCZ. These investigators hypothesized that the ITCZ can serve as a major moisture source for subsequent MJOs.

Ruppert and Johnson (2015) used high-time-frequency sounding and radar measurements from DYNAMO to describe the diurnal cycle of shallow convection during the suppressed phase (SP) of the MJO. They found that daytime convective-cloud deepening and moistening of the lower troposphere was promoted by a combination of daytime increased sea surface temperature (SST) and reduced large-scale subsidence. The importance of such upper-ocean "diurnal warm layers" for invigorating convection has also been noted by others (Chen and Houze 1997; Sui et al. 1997; Johnson et al. 2001; Bellenger et al. 2010; Johnson and Ciesielski 2017). Ruppert and Johnson (2016) conducted large-eddy simulations of this regime to investigate the specific influences of diurnal changes in SST and large-scale subsidence, wherein they parameterized subsidence using the weak temperature gradient (WTG) scheme of Herman and Raymond (2014). Through similar simulations, Ruppert (2016) found that this diurnal cycle of shallow convection drives greater daily mean precipitation, convective heating, and rising motion than would otherwise occur, in turn accelerating the local onset of deep convection. Given the potential importance of such a diurnal time-scale
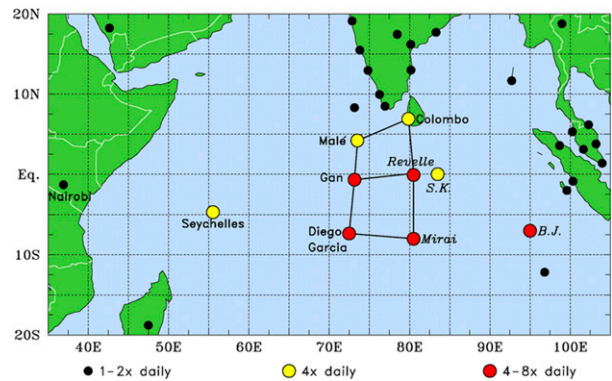

FIG. 1. Map showing the DYNAMO enhanced sounding network with color coding of dots indicating frequency of soundings during the SOP. Note that soundings at *Sagar Kanya* (*SK*) and *Baruna Jaya* (*BJ*) sites were available only for short periods during the SOP.

feedback, there is an imperative to resolve the driving mechanism(s) for diurnal changes in large-scale vertical motion. The hypothesis of Ruppert and Johnson (2015, 2016) that this diurnal cycle was remotely forced by the ITCZ will be tested herein.

A significant component of the DYNAMO observational network involved an enhanced network of upper-air sounding sites over the central IO (Fig. 1) composed of two quadrilateral arrays—one north and one south of the equator—referred to as the northern and southern sounding arrays (NSA and SSA, respectively). During the special observing period (SOP) of the experiment (1 October to 30 November 2011), these sites took 4–8 soundings per day. In this study we make use of this dataset to investigate the diurnal cycle of convection during the suppressed phase of the October MJO in which ITCZ convection was located across the SSA. This paper is organized as follows: section 2 describes the data products used in this study, section 3 focuses on the mean and diurnal characteristics of convection and the attendant flow fields during this period, section 4 explores radiative and convective influences on the ITCZ circulation, and section 5 summarizes the results.

2. Data and analysis procedures

Gridded analyses of large-scale fields were used on a 1° grid with 25-hPa vertical and 3-h temporal resolution covering the domain 20°N–20°S, 35° –155°E. These fields, constructed using multiquadric objective analyses (Nuss and Titley 1994), are referred to here as the CSU V3b (Colorado State University version 3b) gridded product. Input to these analyses came primarily from quality-controlled, bias-corrected, high vertical-resolution sounding data (Ciesielski et al. 2014a). A procedure was developed to mitigate heat

island and flow blocking effects on Colombo sounding data (Ciesielski et al. 2014b) due to the mountainous terrain of Sri Lanka. While sites in the SSA took 3-hourly soundings during the SOP (Fig. 1), the Malé and Colombo sites generally had soundings every 6 h (at 0000, 0600, 1200, and 1800 UTC). To generate a 3-hourly frequency at these latter sites, that is, to create pseudo soundings at 0300, 0900, 1500, and 2100 UTC, a linear interpolation was made between the 6-hourly soundings. To test the accuracy of this approach, the same procedure was carried out at Gan, where 3-hourly soundings were actually taken. Comparison of interpolated soundings with actual soundings indicates an estimated uncertainty of the time-interpolated fields of 0.5°C, 0.5 g kg^{-1}, and 1 m s^{-1} for temperature, specific humidity, and wind speed, respectively. In creating the gridded analysis product, the sounding data were supplemented with satellite-derived winds, scatterometer surface winds, and radio occultation–derived thermodynamic fields. ECMWF operational analyses (OA) were used to augment the objective analyses in the large data void regions outside the core sounding array and when the *Revelle* and *Mirai* research vessels were offsite. However, for the regions and periods considered in this study, the ECMWF OA had little, if any, impact on the analyses within the sounding arrays. The ECMWF OA were also used for analysis of the velocity potential field, which covered a domain larger than the CSU V3b product. Additional details on the supplementary data sources mentioned above can be found in Johnson et al. (2015).

Other datasets used in this study include column-averaged (surface to 200 hPa) all-sky radiation estimates provided by the Clouds and the Earth's Radiant Energy System (CERES) product at 3-h resolution on a 1° grid (Wielicki et al. 1996). Vertical profiles of longwave and shortwave heating rates over Gan Island (Fig. 1) for both clear and all-sky conditions were obtained from the Pacific Northwest National Laboratory (PNNL) Combined Retrieval (CombRet) product (Feng et al. 2014). Combining the all-sky and clear retrievals gives us an estimate of the cloud radiative forcing (CRF). Satellite-estimated rainfall data were from the TRMM 3B42 V7 product at 0.25°, 3-h resolution (Huffman et al. 2007). Radar rainfall data from the *Mirai*, *Revelle*, and Gan-S-Pol at 10-min resolution covering a 320 km × 320 km domain at each site were obtained from the DYNAMO legacy data archive and averaged into 3-hourly bins to facilitate comparison with other datasets at this temporal resolution. In addition, radar-derived stratiform rain fraction (SF), with categorization into rainfall type described in Powell et al. (2016), was available at the *Mirai*. Here SF was computed as (stratiform rain/total rain),
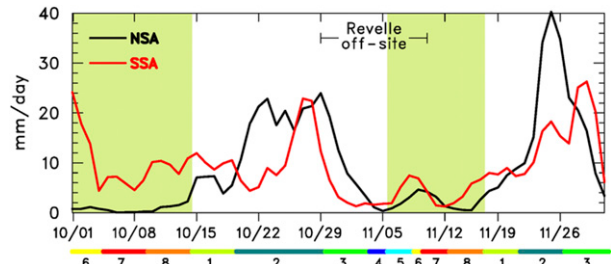

FIG. 2. Time series of 3-day running mean TRMM 3B42 rain rate (mm day^{-1}) averaged over the NSA (black) and SSA (red). Light green shading denotes suppressed periods of the RMM index from 5 to 8. The focus of this study is on the October suppressed period when ITCZ convection was located over the SSA with suppressed conditions and little rainfall over the NSA. The R/V *Revelle* was off-site from 29 October to 10 November. The RMM MJO index is shown along the bottom of the figure.

where stratiform rain did not include any contributions from the isolated convective cells and uncertain categories. As a result, the SF values to be shown are lower by ~20% than those reported in earlier studies (e.g., Xu et al. 2015), but their diurnal trend is similar if contributions from these other "less certain" stratiform categories are included.

For the results to be shown, we define the column-integrated diabatic heating following Yanai et al. (1973) as

$$\langle Q_1 \rangle = LP_o + S + \langle Q_r \rangle = \langle Q_{conv} \rangle + \langle Q_r \rangle, \quad (1)$$

where $\langle () \rangle$ is the vertical integral from the tropopause pressure level p_T to the surface pressure p_S, Q_1 the diabatic heating, Q_{conv} the convective heating, S the surface sensible heat flux, P_o the surface precipitation, L the latent heat of vaporization, and Q_r the net (shortwave + longwave or SW + LW) radiative heating rate. Terms in (1) have the units of watts per meter squared, but for display purposes they are multiplied by the factor $g/[c_p(p_S - p_T)]$ to present them in units of kelvins per day, where g is the acceleration of gravity and c_p is the specific heat of dry air at constant pressure.

3. Results

a. Rainfall characteristics during the DYNAMO SOP

The SOP rainfall time series averaged over each sounding array is shown in Fig. 2 along with the real-time multivariate MJO (RMM) index (Wheeler and Hendon 2004). This index identifies 25 days (highlighted with light green shading) during the SOP as suppressed (phases 5–8) over the IO. While rainfall was light over the NSA during these SPs, the MJO active phases (1–3)

TRMM rainfall (mm/day) for October suppressed period

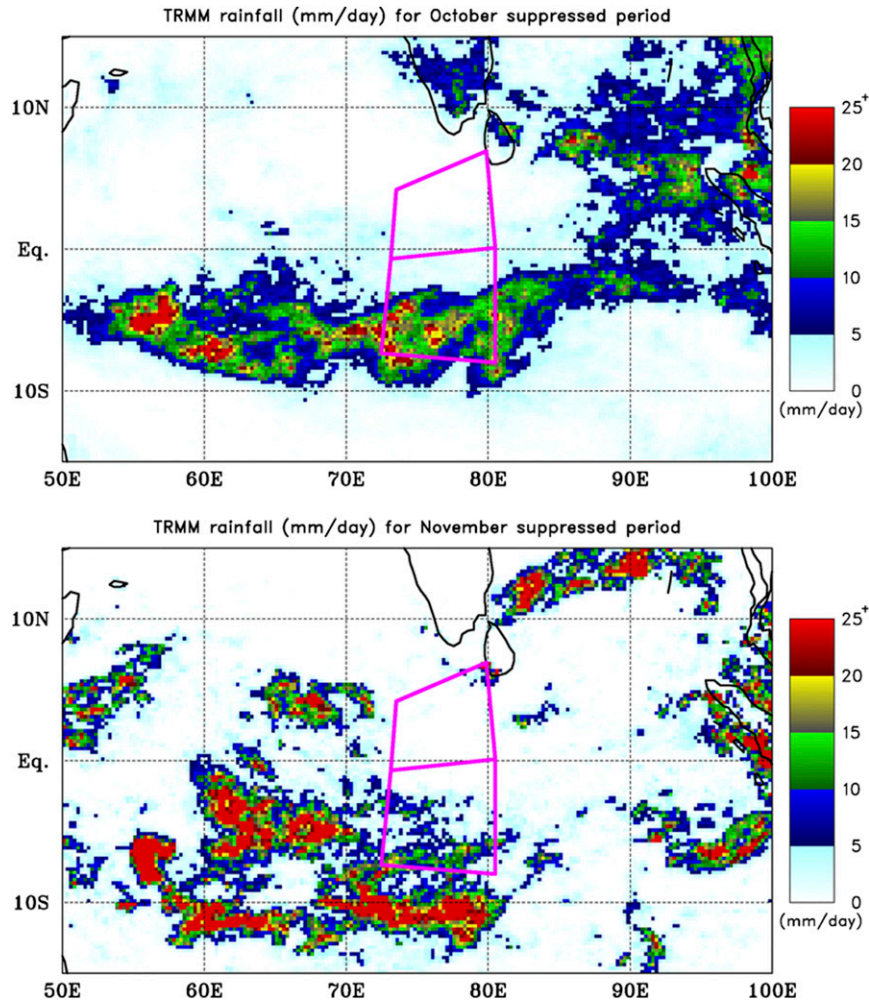TRMM rainfall (mm/day) for November suppressed period

FIG. 3. (top) Rainfall map based on TRMM 3B42v7 product for the 14-day period from 1 to 14 October 2011. (bottom) As in the top panel, but for the 11-day period from 6 to 16 November 2011. Outline of enhanced sounding arrays is shown in magenta. The color scale for rainfall (mm day^{-1}) is on the right.

were characterized by heavy rainfall over both arrays (Gottschalck et al. 2013). Of these 25 suppressed days, 14 occurred prior to the October MJO active phase, with 11 prior to the November active phase.

The associated TRMM rainfall maps for these two periods are shown in Fig. 3. While the October SP was characterized with a single well-established ITCZ band extending across much of the IO south of the equator, convection during the November SP was less organized, with a zonally elongated band of convection south of 10°S and scattered convection west of 70°E. Roughly the first half of the November SP also had a degraded sounding network with the *Revelle* being off-site until 10 November (Fig. 2). Since the rainfall maximum during the October SP laid across the SSA, this 14-day October period will be the focus of this study, in which

3-h observations from the enhanced sounding network are used to examine the circulation structure and diagnostic fields associated with this ITCZ band of convection.

Another perspective on the convection during the SOP can be seen in Fig. 4, which shows a time–latitude plot of rainfall and midlevel vertical motion, both averaged over the longitudes of the enhanced sounding arrays. While rainfall was strongly suppressed over the NSA during the October SP (also seen in Fig. 2), the SSA during this period was characterized with persistent midlevel upward motion and several (at least five) pulses of heavy rainfall at 3–4-day intervals with peaks on 2, 6, 9, 11, and 14 October. Near the end of the October SP, upward vertical motion and rainfall appeared to expand northward from the ITCZ band between 5° and 10°S to a more equatorial position (Johnson and Ciesielski 2013;

Xu et al. 2015). Furthermore, the time–longitude plot of TRMM rainfall over the SSA (not shown) suggests, at times, a slight westward propagation of rainfall features within the ITCZ band consistent with the weak, but deep, easterly flow over this region (Fig. 5a).

b. Mean flow characteristics of October suppressed period

Using the CSU gridded analysis product, north–south cross sections have been created of the mean circulation and diagnostic fields averaged from 72° to 80°E during the October SP (Fig. 5). During this period, ITCZ convection was primarily situated between 5° and 10°S (Fig. 3). Deep easterlies were present in this zonal band (Fig. 5a), potentially indicative of vertical momentum transport by deep convection. The other latitudes exhibit a first baroclinic mode structure with zonal wind reversals in the vertical, with westerlies (easterlies) underlying strong easterlies (westerlies) to the north and south, respectively, of the ITCZ. Reversals are also observed in the meridional winds (Fig. 5b), resulting in low-level convergence and upper-level divergence peaking near 7°S (Fig. 5c) and a broad region of deep rising motion between the equator and 11°S (Fig. 5d). A shallow meridional return flow from the Southern to the Northern Hemisphere was present near 500 hPa (Fig. 5b). Similar shallow meridional circulations have been observed over the ITCZ in the eastern Pacific and in other monsoon regions (Zhang et al. 2004, 2008). On either side of the ITCZ, compensating sinking motion was present throughout the troposphere. Unlike idealized zonally symmetric models in which the ITCZ is coincident with converging low-level northerlies and southerlies (Hack et al. 1989; Schubert et al. 1991), here the low-level convergence resulted from a rapid deceleration of the southerlies with a portion of this flow extending beyond the ITCZ northward into the NH (Fig. 5b). The $\partial u/\partial x$ term had no significant contribution to the low-level divergence field in the ITCZ region. The structures depicted here have the general characteristics of a local Hadley circulation with the primary focus of this study being the cross-equatorial cell.

The large-scale, upper-level flow during the October SP can be visualized in Fig. 6, which shows the 200-hPa divergence and velocity potential field over an extended portion of the Eastern Hemisphere which includes the IO. Here the velocity potential χ is computed from the ECMWF OA divergence field δ shown in Fig. 6a using the relationship $\nabla^2\chi = \delta$. The minimum in χ over the Indonesian/South China Sea region corresponds to a broad area of convectively disturbed weather and upper-level divergence. This pattern is distinct from the continental-scale Asian
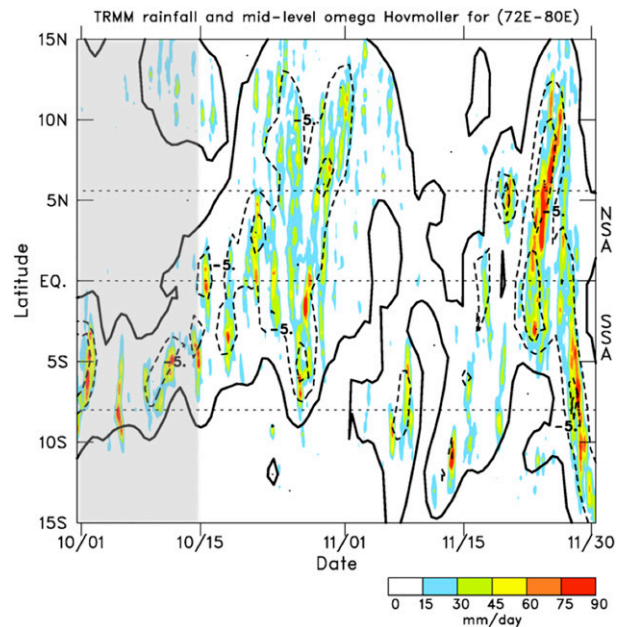

FIG. 4. Hovmöller plot for daily averaged TRMM 3B42 rainfall (mm day^{-1} with color scale at bottom) and midlevel (400–500 hPa) vertical motion (contoured with interval 5 hPa h^{-1}) averaged over 72°–80°E for the DYNAMO SOP period. Heavy solid line is the zero contour of vertical motion. Latitudinal limits of enhanced sounding arrays are shown with horizontal dashed lines. The October SP is indicated with light gray shading.

summer monsoon mode observed by Krishnamurti and Kishtawal (2000), which had a strong diurnal signal centered over southern India. In Fig. 6b, the ITCZ region between 5° and 10°S is characterized as a trough of lower χ values. Divergent flow, which is perpendicular to isolines of χ, was present within the ITCZ as a region of upper-level outflow. In addition, divergent flow associated with convection over Indonesia contributed to the strong upper-level easterlies seen in Fig. 5a over the NSA. While zonal winds contributed little to the low-level divergence pattern over the ITCZ (Fig. 5c), at 200 hPa they account for a significant fraction (>50%) of the convergence observed over the NSA as surmised from the χ pattern over this region (Fig. 6b). Therefore, the ITCZ-related local Hadley cell over the IO during this period was not an isolated phenomenon, but rather its circulation was superimposed on that of the large-scale east–west flow pattern depicted in Fig. 6.

The associated apparent heating Q_1 and apparent drying Q_2 fields (Yanai et al. 1973) are shown in Figs. 5e and 5f. The large vertical separation between the peaks in Q_1 and Q_2 is indicative of vigorous deep convection within the ITCZ (Yanai et al. 1973). Outside this region tropospheric deep cooling related to radiative effects and low-level moistening (negative Q_2 maxima) associated with shallow, lightly
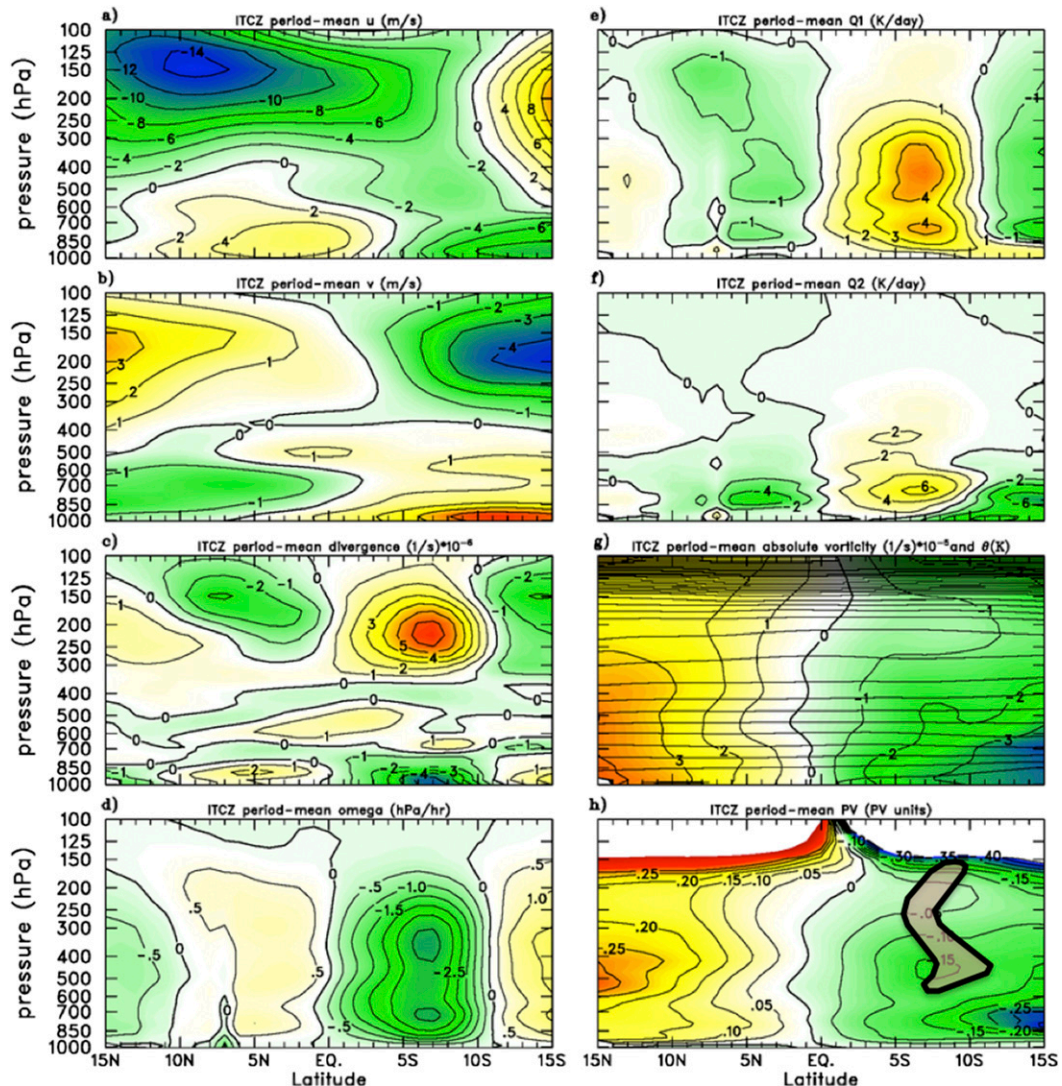
FIG. 5. ITCZ period-mean (1–14 Oct 2011) latitudinal cross section averaged over 72°–80°E for (a) zonal wind field, (b) meridional wind field, (c) divergence, (d) vertical p velocity, (e) apparent heating, (f) apparent drying, (g) absolute vorticity (color) and potential temperature (contours with 5-K increment), and (h) potential vorticity. In Fig. 5h the shaded region represents the area where the meridional PV gradient is reversed, satisfying the Charney–Stern necessary condition for combined barotropic–baroclinic instability.

precipitating convection can be seen. Reasons for the double maximum in vertical motion (Fig. 5d) and the heating field (Fig. 5e) within the ITCZ will be considered later. Finally, potential vorticity (PV) and its companion fields—absolute vorticity and potential temperature θ—are shown in Figs. 5g and 5h. Layers of enhanced stability, indicated by a tightening of the vertical θ gradient, result in regions of higher PV such as in the tropopause region (above 200 hPa) and south of 10°S near 800 hPa, where a signature of the trade-wind inversion layer can be seen (Schubert et al. 1995). Advection of PV by the meridional wind resulted in regions near the equator where the condition for inertial

instability was satisfied ($f \times PV < 0$, where f is the Coriolis parameter; Stevens and Ciesielski 1986). Also, the shaded region of PV in Fig. 5h represents a region in which latent heat released within the ITCZ resulted in a reversal in the meridional PV gradient, which satisfies the necessary condition for combined barotropic–baroclinic instability (Charney and Stern 1962; Eliassen 1983). This instability can result in ITCZ breakdown (Nieto Ferreira and Schubert 1997; Wang and Magnusdottir 2005) and may offer a possible explanation for the 3-day pulses of the ITCZ convection seen in Fig. 4. Using reanalysis datasets, Duvel (2015) found that reversals in the meridional gradient of PV around
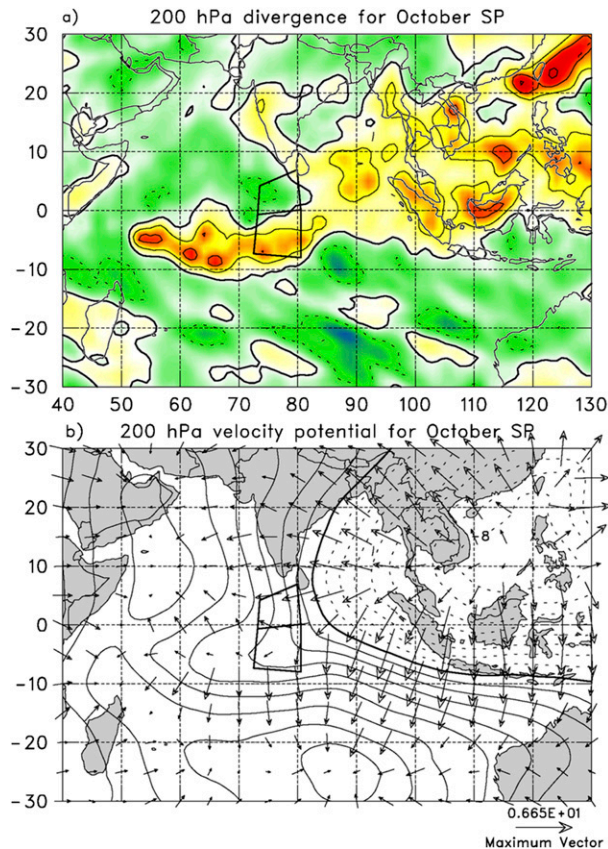
FIG. 6. (a) October SP-mean 200-hPa divergence (warm shading shows areas of divergence, cool shading areas of convergence with contour increment of 5×10^{-6} s^{-1}, and heavy line is zero contour). (b) As in (a), but for velocity potential (contours in units of 10^6 m^2 s^{-1}) with divergent wind field (vectors with scale at bottom).
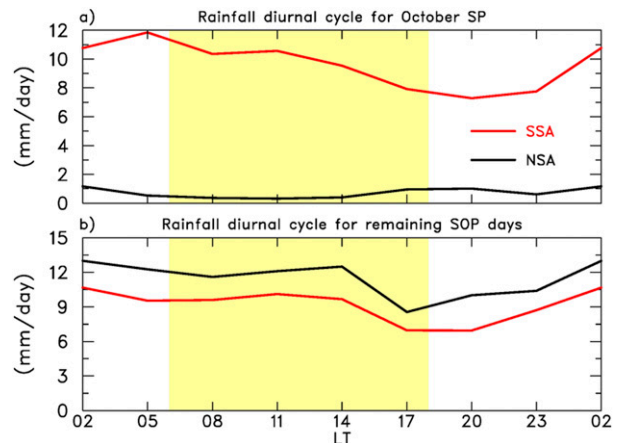

FIG. 7. (a) Diurnal cycle of TRMM 3B42 rainfall over NSA (black) and SSA (red) for the October suppressed period when the ITCZ was present over the SSA. (b) As in (a), but for the remaining 47 days during the DYNAMO SOP. Yellow shading denotes daylight hours.

10°S over the IO were the likely cause for instabilities that lead to tropical depression initiation. An alternative explanation for at least some of the pulses in ITCZ rainfall could be the presence of convectively coupled waves (Dias and Pauluis 2009) since westward propagating equatorial Rossby waves were observed over the IO during this October period (Gottschalck et al. 2013, their Fig. 13).

c. Diurnal characteristics of convection and attendant flow during October suppressed period

We now leverage the eight per day sampling of observations during the October SP to examine the characteristics of the diurnal cycle. The diurnal cycle of TRMM rainfall was largely out of phase between the NSA and SSA during the October SP (Fig. 7a). Over the SSA, rainfall peaked at 0500 LT with broad minimum between 1700 and 2300 LT. The diurnal rainfall range over the SSA was 4.7 mm day^{-1}, or about 50% of period mean rate of 9.7 mm day^{-1}. In contrast, the NSA was

characterized by very light rainfall[2] with a broad morning minimum and weak evening maximum of ~1 mm day^{-1}. For context, on the remaining 47 SOP days (a combination of 11 convectively suppressed and 36 active days), rainfall over both arrays was similar with an overnight 0200 LT maximum and 1700–2000 LT minimum (Fig. 7b). This is generally consistent with the findings of Sakaeda et al. (2017), who found an early morning rainfall peak (0300 LT) over the central IO (their Fig. 1c) based on 11 years of boreal winter TRMM rainfall data.

A latitudinal cross section of rainfall over the longitudes of the sounding arrays (72°–80°E, Fig. 8) for the October SP clearly shows large diurnal changes in rainfall over the ITCZ region, with peak rates decreasing from over 20 mm day^{-1} in the early morning to around 10 mm day^{-1} in the early evening. A small evening rainfall increase over the NSA was confined to within a few degrees of the equator. Using radar data from the two near-equatorial sites, Gan and *Revelle*, a comparison is made between the diurnal cycle of radar rainfall to that from TRMM at these sites for the October SP (Fig. 9). The radar domains for these two sites lie outside the active precipitation area within the SSA. During this light rainfall period, TRMM substantially underestimated (by 30%–50% in the mean) radar values

---

[2] The light rain rates over the NSA seen in Fig. 7a should be regarded with some caution as the TRMM product underestimates light rainfall due to the sensitivity of the TRMM sensors (i.e., it undersamples shallow, warm-rain clouds; Xu and Rutledge 2014; Ciesielski et al. 2017).
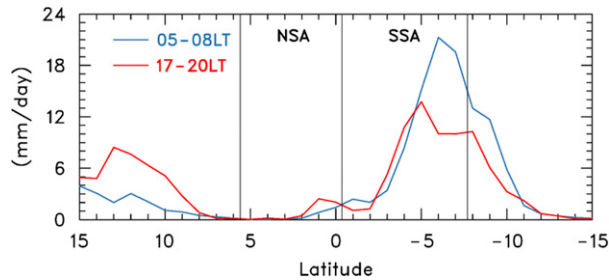
FIG. 8. Latitudinal cross section of TRMM 3B42 rainfall averaged over 72°–80°E for 0500–0800 LT (blue) and for 1700–2000 LT (red). Light vertical lines show latitudinal limits of the enhanced sounding arrays.
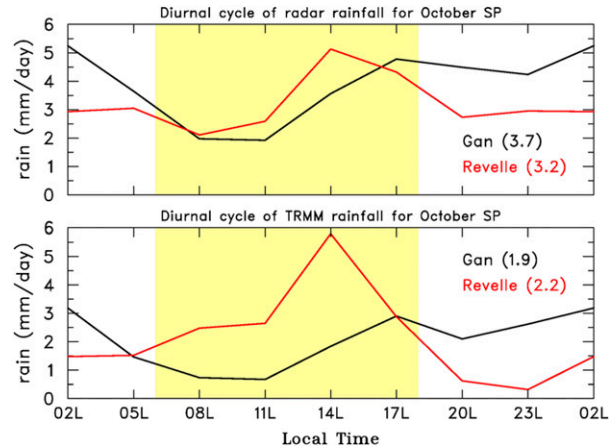

FIG. 9. (top) Diurnal cycle of radar rainfall during the October suppressed period for Gan (black) and *Revelle* (red); (bottom) as in top panel, but from TRMM-3B42 product. Values in parentheses represent the period means. Yellow shading denotes daylight hours.

at both locations, consistent with the findings from previous studies (Xu and Rutledge 2014; Ciesielski et al. 2017). The rainfall maximum at the *Revelle* occurred at 1400 LT in both estimates, with Gan having a relative maximum at 1700 LT and slightly higher peak at 0200 LT. The coexistence of both afternoon and nocturnal peaks in clouds and precipitation in the DYNAMO suppressed regimes was also noted by Ruppert and Johnson (2015) and Johnson and Ciesielski (2017, their Fig. 13b). In the former study, it was argued that the afternoon–evening peak in rainfall (1400–1700 LT) is linked to locally warmer daytime SSTs (Bellenger et al. 2010), higher surface fluxes, and relaxed large-scale subsidence. The present study suggests that diurnal changes in the Hadley circulation (detailed next) were contributing to the afternoon rainfall peak. The nocturnal peak may be related to either propagating tides (Woolnough et al. 2004) and/ or diurnal radiative feedback mechanisms, such as those described by GJ77 and Randall et al. (1991). The presence of the nocturnal peak at Gan and its absence at the *Revelle* suggests that regional differences in the thermodynamic state and/or the circulation existed between these sites during the October SP. Examination of these differences is beyond the scope of this study.

Associated with these diurnal rainfall variations, Fig. 10 shows the morning (0500–0800 LT) and evening (1700–2000 LT) vertical cross sections of several diagnostic fields. These times were chosen since analysis differences between them were most pronounced and generally correspond to the times of the diurnal rainfall extremes seen in Fig. 7a. Low-level (surface to 850 hPa) convergence in the ITCZ region and low-level divergence over the NSA weakened going from morning to evening (Figs. 10a,e). This results in prominent diurnal pulsing in vertical motion (Figs. 10b,f) with much stronger rising (sinking) motion within the ITCZ (over the NSA) in the morning hours. Over the NSA, strong early morning subsidence gave way to weak subsidence in the evening hours and even slight upward motion,

most notably between the equator and 2°N, consistent with evening rainfall increase seen in Figs. 8 and 9. The diurnal amplitude of vertical motion over the NSA was ~1.0 hPa h^{-1}, which is about half that observed in the trade-wind environment during BOMEX (Table 1; Nitta and Esbensen 1974). The corresponding apparent heating fields (Figs. 10c,g) reflect this diurnal pulsing, with morning heating rates in the ITCZ region being nearly double those in the evening. A notable difference in the apparent drying fields (Figs. 10d,h) is the deeper moistening signature in the evening hours over the NSA consistent with the relaxed subsidence during this time and reflecting the moistening effects associated with daytime growth of the cumulus cloud field (Ruppert and Johnson 2015). This moistening is important in the transition from shallow to deep convection leading into the MJO convective phase (Johnson et al. 2015; Xu and Rutledge 2016). In summary, these analyses depict a diurnally pulsing Hadley circulation that ran stronger in the early morning hours, resulting in peak rainfall in the ITCZ region during this time. This diurnal cycle is consistent with previous findings (GJ77; Hendon and Woodberry 1993; Deser and Smith 1998). In addition, the daytime reduction in subsidence over the NSA within the subsiding branch of the cross-equatorial Hadley cell allowed shallow convection and associated moistening to deepen during the pre-onset stage of the MJO.

Figure 11 provides another perspective on the north–south out-of-phase relationship in the low-level divergence and deep-layer (DL; 850–200 hPa) vertical motion and their diurnal changes during the October SP. Low-level convergence peaked in the ITCZ near
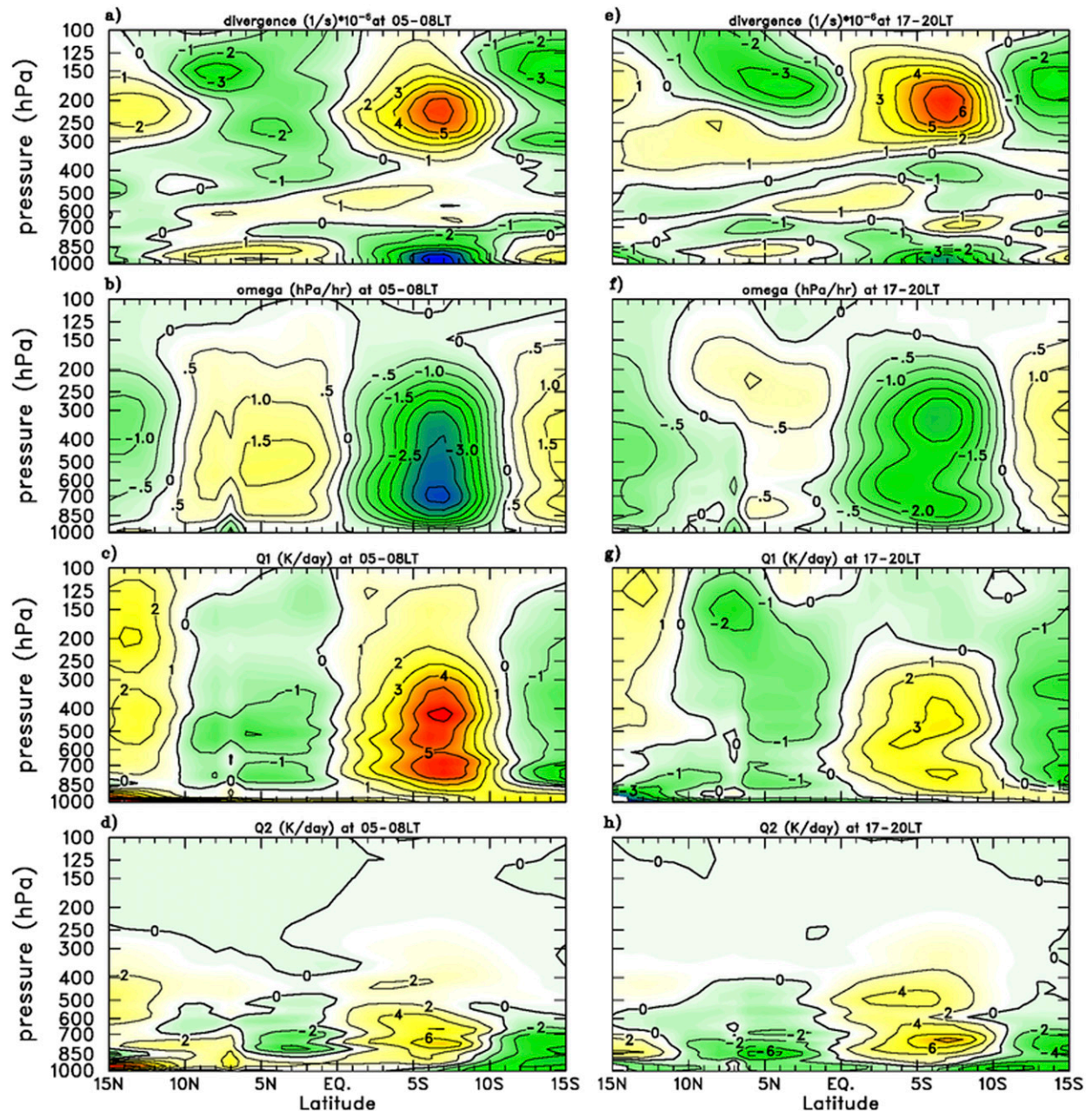
FIG. 10. October SP-mean latitudinal cross section averaged over 72°–80°E for (a) divergence at 0500–0800 LT, (b) omega at 0500–0800 LT, (c) apparent heating at 0500–0800 LT, (d) apparent drying at 0500–0800 LT, (e) divergence at 1700–2000 LT, (f) omega at 1700–2000 LT, (g) apparent heating at 1700–2000 LT, and (h) apparent drying at 1700–2000 LT.

7°S at 0500 LT, while low-level divergence peaked over the NSA a few hours on either side of this time (Fig. 11a). As the low-level ITCZ convergence weakened going into the evening hours, low-level divergence over NSA weakened in concert. Tied to these low-level divergence changes through mass-continuity considerations, upward vertical motion peaked in the ITCZ in the early morning hours with a maximum in compensating subsidence over the NSA near this time (Fig. 11b). Likewise, the minimum in upward motion in the ITCZ region from 1700 to 2300 LT, which is consistent with the diurnal timing of vertical motion during the convectively active periods in TOGA COARE (Sui et al. 1997; see Table 1), coincided with the period of weakest subsidence over the NSA.
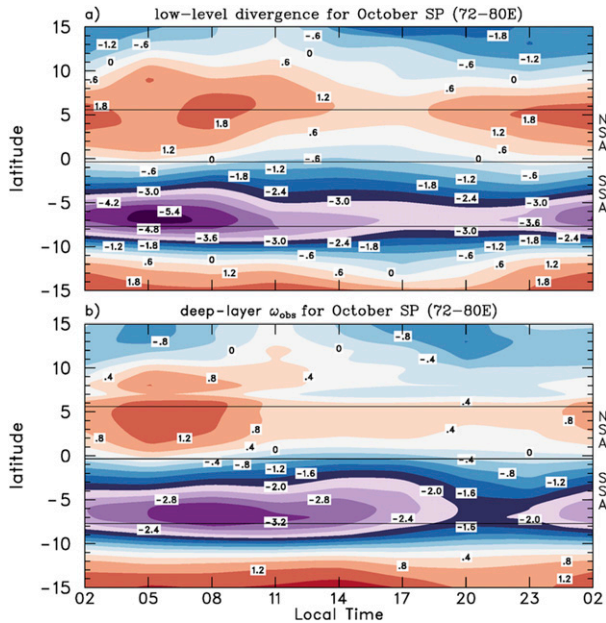
FIG. 11. (a) Latitudinal cross section averaged over 72°–80°E showing diurnal variation of the low-level (surface to 850 hPa) divergence ($\times 10^{-6}\,\mathrm{s}^{-1}$ with contour interval of $0.6 \times 10^{-6}\,\mathrm{s}^{-1}$) for October suppressed period. (b) As in (a), but for observed deep-layer (850–200 hPa) vertical motion (hPa h^{-1} with contour interval of 0.4 hPa h^{-1}). Latitudinal limits of enhanced sounding arrays are shown with light horizontal lines.

d. Longer-term context for October SP

As noted earlier, Zhang and Sodowsky (2016) identified 205 ITCZ events lasting 2 days or longer over the IO region (60°–90°E) using TRMM rainfall products from 1998 to 2013. Using the TRMM rainfall record for this same period, we examine whether convective conditions similar to the October SP were present in other years by averaging rainfall over the sounding array areas. Since the SSA to NSA ratio of 1:2:1 filtered daily rainfall was greater than 4 for each day during the October SP indicating persistent heavier rainfall over the SSA (Fig. 2), we examine the diurnal cycle of rainfall on all days in which this threshold ratio was exceeded for six or more consecutive days over either of the arrays. Using these criteria, we identified 19 (95) cases with heavier rainfall over the NSA (SSA), with average length of these cases being 7.8 (8.8) days for the NSA (SSA). Considering the number of cases in each region and their average length, this translates into an occurrence rate for these conditions of 9.3 days yr^{-1} (or 2.5% of days) over the NSA and 52.3 days yr^{-1} (or 14.3% of days) over the SSA. Over the array with heavier rainfall, its diurnal cycle (not shown) is remarkably consistent to that seen in Fig. 7a, with a similar diurnal amplitude ($\sim$3.5 mm day^{-1}) and a maximum (minimum) at 0500 LT

(2000 LT). Over the array with suppressed convection, a weak rainfall diurnal cycle (amplitude <0.4 mm day^{-1}) is present and is also similar to Fig. 7a with a morning (0800–1100 LT) minimum and slight peaks at 1700 and 0200 LT (not shown). While it is unclear from this analysis whether the array with the heavier rainfall contained an ITCZ, the strong diurnal cycle in rainfall in the active region and its out-of-phase relationship to the suppressed region suggests that a diurnally pulsing "Hadley cell–like" circulation, similar to that observed in the October SP, was present 15%–20% of the time over IO in this 16-yr record.

4. Radiative and convective influences on the ITCZ circulation

a. Observations of deep-layer convective and radiative heating

To assess what mechanisms may be influencing the circulation features during the October SP and their diurnal changes, Fig. 12 examines the diabatic forcing fields, specifically, the diurnal variations in DL convective heating $<Q_{\mathrm{conv}}>$ and in all-sky column net radiation $<Q_r>$. Here $<Q_{\mathrm{conv}}> = <Q_1> - <Q_r>$ is computed using the CSU gridded analysis product and CERES Q_r data, where $<()>$ is from 850 to 200 hPa yielding a DL average.[3] The parameter $<Q_{\mathrm{conv}}>$ varied within the ITCZ region from a maximum of $\sim$5 K day^{-1} near 0500 LT to a minimum of 2.7 K day^{-1} at 2000 LT (Fig. 12a). The 0500 LT peak in $<Q_{\mathrm{conv}}>$ is consistent with the timing of peak rainfall over the SSA (Fig. 7). Over the convectively suppressed NSA, there was a slight uptick in $<Q_{\mathrm{conv}}>$ after 1100 LT. This increase, which maximized at $\sim$0.5 K day^{-1} in the evening hours (1700–2000 LT), is particularly noticeable between the equator and 2°N. North of the NSA, the larger midday increase in $<Q_{\mathrm{conv}}>$ was associated with deeper land convection over Sri Lanka and southern India. In comparison, the diurnal amplitude of $<Q_r>$ was $\sim$2 K day^{-1} at all latitudes (Fig. 12b), with enhanced radiative heating due to cloud and moisture effects in the ITCZ region and stronger nighttime cooling both north and south of the SSA convectively active zone. Using a simplified zonally symmetric model, Raymond (2000) has argued that differential radiative heating between

---

[3] Since CERES does not provide Q_r estimates at 850 hPa, the CERES $<()>$ was from the surface to 200 hPa. However, integration of Q_r from the surface to 200 hPa yields virtually identical results to integration from 850 to 200 hPa, as determined from radiative profiles from Gan Island during DYNAMO (Fig. 10 of Johnson et al. 2015).
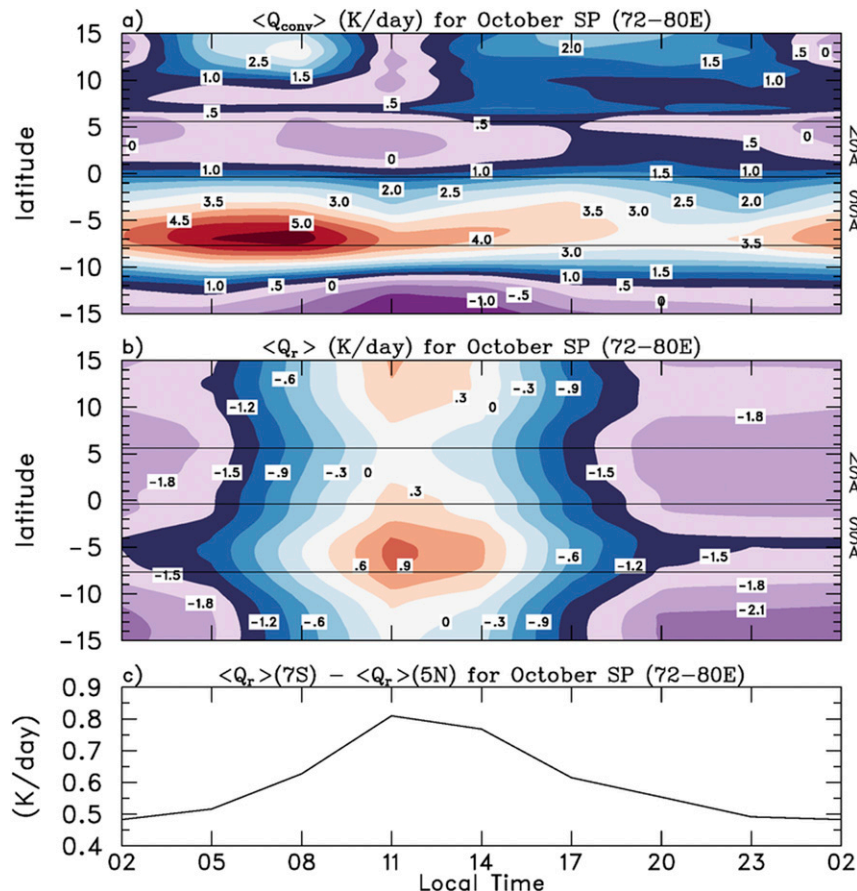
FIG. 12. (a) Latitudinal cross section averaged over 72°–80°E showing diurnal variation of DL (850–200 hPa) convective heating $<Q_{conv}>$ (K day^{-1} with contour interval of 0.5 K day^{-1}) for October suppressed period. (b) As in (a), but for DL (surface to 200 hPa) radiative heating (K day^{-1} with contour interval of 0.3 K day^{-1}), (c) meridional gradient of $<Q_r>$ between sounding arrays shown as $<Q_r>$ at 7°S minus $<Q_r>$ at 5°N. Latitudinal limits of enhanced sounding arrays are shown with light horizontal lines in (a) and (b).

cloudy and clear regions, such as depicted in Fig. 12c, is sufficient to lead to an instability that results in a cross-hemispheric Hadley circulation.

b. Possible factors influencing diurnal cycle of the ITCZ

Determining the detailed impacts of these forcing fields on the circulation would require numerical simulations that are beyond the scope of this study; however, we consider a related but important question: What processes control the diurnal cycle of vertical motion within the ITCZ circulation (as depicted in Figs. 10b, 10f, and 11b)? In a recent modeling study, Ruppert and Hohenegger (2018) found that the diurnal cycle of overturning motion associated with organized deep convection maintains approximate WTG balance (Sobel et al. 2001). Specifically, they find that on scales up to $O(10^3)$ km (roughly the scale of the sounding arrays),

the adjustment of the circulation toward WTG balance through propagating gravity waves occurs rapidly relative to the diurnal cycle. Here, we examine the degree to which WTG balance holds in relation to the daily mean and diurnal variation of the observed deep-layer vertical motion ω_{obs} during the October SP. GJ77 argued that the diurnal cycle of organized convection is driven by diurnal variations of overturning motion related to differential radiative heating between clear and cloudy areas. This argument, which essentially invokes WTG balance, is tested below.

WTG balance takes the form

$$
\begin{aligned}
\omega &\approx Q_1 \Big/ \left[\left(\frac{T}{\theta} \right) \frac{\partial \theta}{\partial p} \right] \\
\omega_{conv} + \omega_r &\approx (Q_{conv} + Q_r) \Big/ \left[\left(\frac{T}{\theta} \right) \frac{\partial \theta}{\partial p} \right],
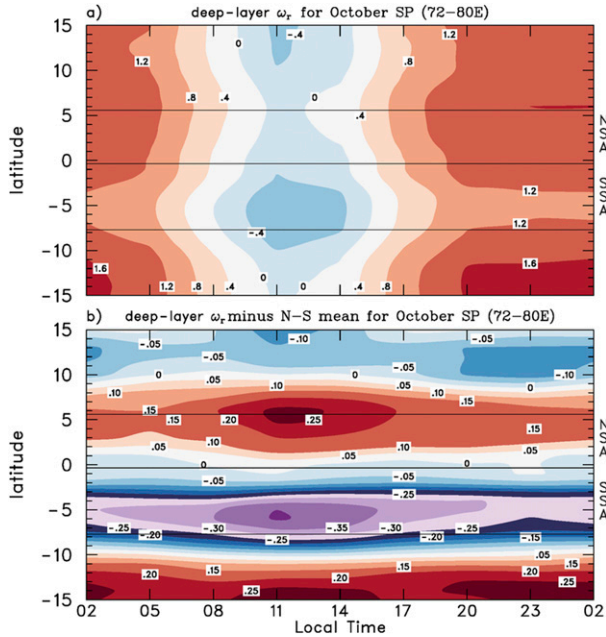\end{aligned}
\tag{2}
$$

FIG. 13. (a) Latitudinal cross section averaged over 72°–80°E showing diurnal variation DL vertical motion due to radiative effects (hPa h^{-1} with contour interval of 0.4 hPa h^{-1}). (b) As in (a), but shown as a deviation from its north–south (N–S) mean at each local time (hPa h^{-1} with contour interval of 0.05 hPa h^{-1}). Here the N–S mean is computed from 15°N to 15°S. Latitudinal limits of enhanced sounding arrays are shown with light horizontal lines.

TABLE 2. Daily mean values of DL (850–200 hPa) WTG vertical motions (hPa h^{-1}) averaged over October SP for various terms in thermodynamic equation for the NSA (0°–3°N) and ITCZ (5°–8°S) regions. (left to right) DL vertical motion resulting from horizontal temperature advection (hta), radiation heating (r), convection heating (conv), sum of convection and radiative heating, and observed. See text for additional details.

Region	ω_{hta}	ω_r	ω_{conv}	$\omega_{\text{conv}} + \omega_r$	ω_{obs}
NSA	0.02	0.83	−0.47	0.36	0.39
ITCZ	0.06	0.48	−3.15	−2.67	−2.62

analysis shows increased relative rising motion at midday due to locally enhanced shortwave heating (Fig. 12b) with increased relative subsidence over the NSA and south of the ITCZ, where daytime radiative heating is weaker. Noteworthy in this deviation ω_r field is that the largest north–south gradient between the ITCZ and the NSA suppressed region occurred during the daylight hours. This is consistent with the analysis in Fig. 12c that shows the gradient in $<Q_r>$ between 7°S and 5°N peaking during the daylight hours. While GJ77 suggested that the radiative gradient between disturbed and clear regions peaks at night, this is clearly not the case during the October SP.

To assess how WTG balance holds during the October SP, Table 2 compares daily mean DL WTG vertical motions to ω_{obs} within the ITCZ (5°–8°S) and the NSA (0°–3°N) regions. Here we include the effect of the horizontal temperature advection (hta) term $v \cdot \nabla T$ which, when normalized by lapse rate, yields ω_{hta} with units of hectopascals per hour. Indeed, from Table 2 we note that, compared to the other terms, ω_{hta} is considerably smaller, supporting the notion of WTG balance in the daily mean state. This conclusion is corroborated by the excellent agreement between $\omega_{\text{conv}+\omega_r}$ and ω_{obs}. Furthermore, the magnitude of ω_{conv} within the ITCZ highlights the importance of convection for the overall strength of rising motion in the ascending branch of the Hadley cell.

To facilitate an assessment of WTG balance within the diurnal cycle, Fig. 14 compares the diurnal variations of the WTG vertical motions with ω_{obs} for the ITCZ and NSA regions. Here the fields are shown as perturbations from their daily means given in Table 2 while ω_{hta} is not included because of its negligible diurnal amplitude in comparison to the other terms. First, considering the NSA region, we note that the reduction in subsidence ω_{obs} from 0500 to 1100 LT over the NSA correlates well with the decreasing subsidence produced by the ω_r field at this time. However, this consistency breaks down over the NSA, particularly between 1400 and 2300 LT when ω_{obs} and ω_r exhibit disparate trends, suggesting that

where ω_{conv} is the DL vertical motion due to convection, ω_r is the DL vertical motion due to radiative effects Q_r, and the denominator is the DL atmospheric lapse rate. Given that lapse rate over the sounding arrays is nearly a constant in the vertical between 850 and 200 hPa (not shown), we limit our analysis to this layer and assume a DL lapse rate value of $-0.054 \, \text{K hPa}^{-1}$. To determine the DL WTG vertical motion associated with radiative effects, we use CERES $<Q_r>$ values.

Analysis of ω_r as a function of local time and latitude for the October SP can be seen in Fig. 13a. As expected, ω_r shows daytime rising motion and nighttime sinking motion in response to daytime shortwave (SW) heating and nighttime longwave (LW) cooling, respectively. Nocturnally enhanced subsidence is evident on either side of the ITCZ, with it being somewhat diminished over the NSA in comparison to that observed south of the ITCZ. To emphasize the regional impacts of Q_r on the circulation, Fig. 13b shows ω_r as a deviation from its north–south (i.e., 15°N–15°S) mean at each local time. This analysis demonstrates that at all times of day the differential radiative warming resulting from the effects of clouds and enhanced moisture in the ITCZ supports the local Hadley circulation, consistent with the arguments of Raymond (2000). Within the ITCZ, this
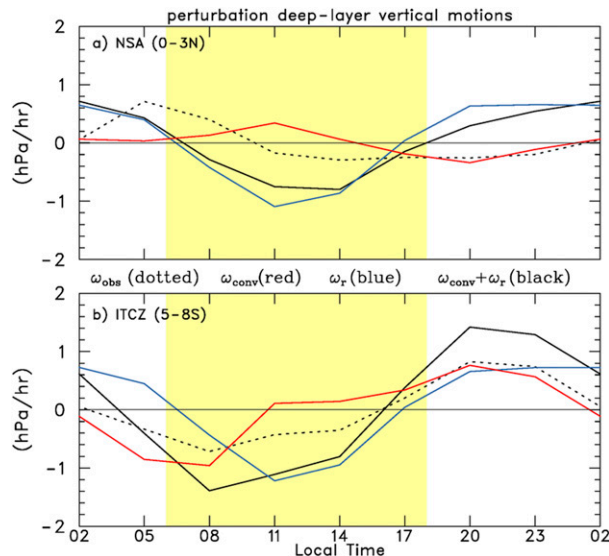
FIG. 14. (a) Diurnal variation of perturbation DL (850–200 hPa) vertical motions (hPa h^{-1}) averaged from 72° to 80°E over a portion of NSA (0°–3°N) for the October suppressed period, and (b) as in (a), but averaged over the ITCZ region (5°–8°S). Observed DL vertical motion (ω_{obs}; dotted), due to convection (ω_{conv}; red), due to radiation (ω_r; blue), and $\omega_{conv} + \omega_r$ (black). Perturbation of fields are from mean values listed in Table 2. Note that difference trends in NSA vertical motions (ω_{obs} and ω_r) between 1400 and 2000 LT suggest that processes other than radiation are impacting vertical motion.

processes other than radiation are playing a significant role. Over the ITCZ region, diurnal trends in the ω_r and ω_{obs} vertical motion fields are generally congruent. For example, the increase in ω_{obs} from 0200 to 0800 LT and its reduction of 1.5 hPa h^{-1} from 1100 to 2000 LT agree well with changes in ω_r over these hours. This correlation breaks down at other times, most notably from 0800 to 1100 LT, when ω_{obs} shows a weakening upward motion at a time when ω_r through SW heating effects suggest a strong opposite trend. A possible explanation for this discrepancy may be the effects of SW heating near cloud top, which would stabilize convection (Randall et al. 1991; Ciesielski et al. 2017) and reduce deep-column upward motion. The decrease in upward motion in ω_{conv} in the same timeframe supports this interpretation. The diurnal changes in ω_{conv} are also congruent with ω_{obs}. Overall, the good correspondence within the ITCZ (Fig. 14b) between the diurnal trends in total WTG vertical motion (black curve) and that observed (dashed curved) suggests that the diurnal cycle of overturning circulation is consistent with a rapid adjustment toward WTG balance. This diurnal cycle in circulation is driven both by diurnal changes in radiative heating and convective heating consistent with the findings of Ruppert and Hohenegger (2018), who argue that the circulation

in tropical organized convection likely maintains approximate WTG balance.

To further explore the diurnal cycle of convection within the ITCZ, Fig. 15 shows the October SP-mean vertical structure of vertical motion and convective heating over the course of a day within the ITCZ (5°–8°S). In both fields there is a dramatic shift from early morning (0200–0500 LT) bottom-heavy profiles to daytime (0800–1700 LT) top-heavy profiles. This daytime shift to top-heavy vertical motion coincided with an increase in convergence around 400 hPa and a divergence increase near 200 hPa (Fig. 10e). GJ77 noted this enhanced daytime midlevel convergence in the convective region and attributed it to diurnal changes in the midlevel horizontal pressure gradient related to SW heating in the upper clouds. The evolution of these fields suggests a transition from convective rainfall at night to more stratiform rainfall during the daytime hours. This diurnal evolution was generally similar to findings from previous field campaigns, for example, the 1978 Winter Monsoon Experiment (Houze et al. 1981; Houze 1982; Johnson and Young 1983).

Since the *Mirai* (positioned at 80°E, 8°S) was on the edge of the ITCZ rainband during this period (Fig. 3a), we use its radar data to analyze the rainfall and stratiform fraction for this location (Fig. 16). The peak radar-derived rainfall at 0500 LT and the evening minimum are consistent with the TRMM diurnal variability over the SSA shown in Fig. 7. The dip in radar rainfall at 0800 LT was not seen in the TRMM rainfall (Fig. 7a), suggesting that sampling issues may be present in this 14-day mean over the limited *Mirai* radar domain. The stratiform fraction (Fig. 16b) had a nighttime minimum, an increase near daybreak, and an early afternoon maximum generally consistent with the evolution of convective heating profiles shown in Fig. 15. Despite the sampling limitations, these radar results corroborate the notion that the ITCZ convection during the October SP underwent a daily evolution from early morning bottom-heavy convective profiles to daytime top-heavy stratiform ones.

A contributing factor in the diurnal evolution of ITCZ convection observed in Figs. 15 and 16 is the effects of daytime SW absorption by clouds. For example, Fig. 17 shows the CRF for LW, SW, and their net (LW + SW) composited by local time of day for rain rates ≥10 mm day^{-1} based on data from Gan Island during DYNAMO (Ciesielski et al. 2017). This rain rate threshold was chosen as it roughly corresponds to the minimum rate within the ITCZ during the October SP (red curve in Fig. 8). The CRF fields in Fig. 17 are representative of ~18 days satisfying this rain rate threshold. At higher rain rates common within the
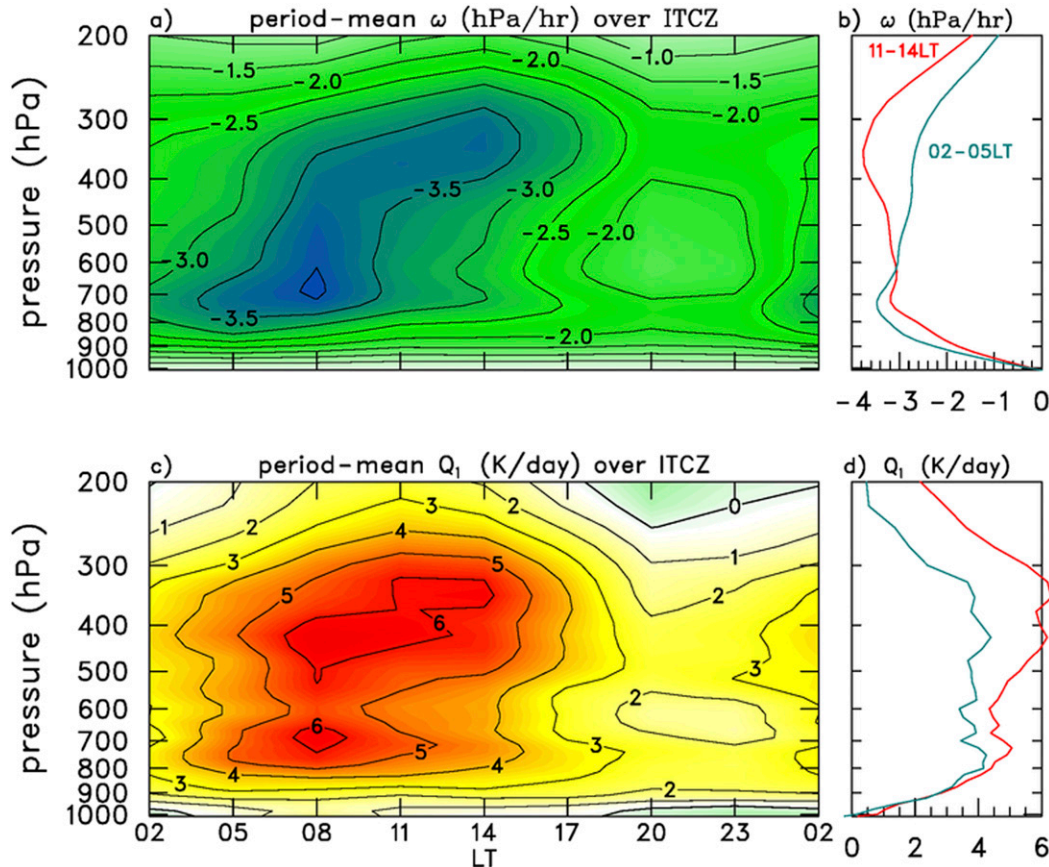
FIG. 15. Mean diurnal cycle over the ITCZ (5°–8°S) for the October SP of (a) vertical motion and (b) mean vertical motion profiles at 0200–0500 LT (cyan) and at 1100–1400 LT (red). (c) As in (a), but for apparent heating Q_1, and (d) as (b), but for mean Q_1 profiles. Fields have been averaged between 72° and 80°E.

ITCZ, the CRF signatures become more intense, as suggested by the CRF versus rain rates composites shown in Ciesielski et al. (2017, their Fig. 6). As seen in Fig. 17c, nighttime hours were characterized by a thin layer of strong LW cooling near 200 hPa with LW heating at low levels. In contrast, daytime conditions show a strong upper-level heating peak slightly below 200 hPa due to SW CRF effects. As noted in Feng et al. 2014, these upper-level peaks in LW cooling and SW heating may in reality occur at a higher altitude due to undersampling of high clouds and cirrus in the CombRet product. Nevertheless, the localized maximum in radiative heating at midday over the ITCZ region apparent in Fig. 12b is focused in upper levels. At nighttime the prevalence of deep clouds in the ITCZ leads to locally enhanced LW cooling from cloud tops and warming in the lower to midtroposphere.

The finding that the rising branch of Hadley circulation adjusted rapidly toward WTG balance throughout the diurnal cycle provides a basis of support for the general hypothesis of GJ77 that diurnally varying differential radiation may directly drive circulation changes. While this important premise of GJ77 appears consistent with our analyses, other aspects of their argument appear deficient. For example, their notion that the radiative diurnal cycle is larger in the suppressed environment relative to regions of disturbed weather is not the case for the October SP. Figures 13b, 14, and 17 reveal that daytime SW heating in the ITCZ region resulted in a larger radiative diurnal amplitude in convective regions $(2.1 \, \text{K day}^{-1})$ relative to areas of suppressed convection (e.g., the NSA; $1.8 \, \text{K day}^{-1})$. Furthermore, GJ77 hypothesized that an enhanced *nighttime* differential radiative gradient (largely due to nighttime LW cooling in suppressed regions) impacts the convective region through mass continuity. On the other hand, while a differential radiative heating gradient that promotes a mass circulation into the ITCZ exist throughout the course of the day, its amplitude is greatest during daylight hours (Fig. 12c), suggesting that the strong CRF at upper levels (Fig. 17b) is stabilizing the lapse rate so as to inhibit deep convection at that
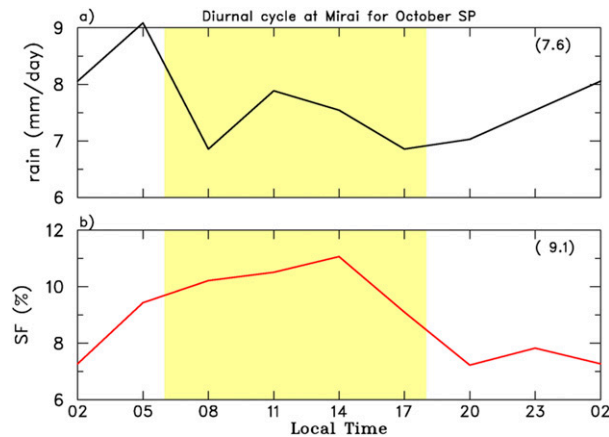
FIG. 16. Diurnal variation of (a) *Mirai* radar rainfall (mm day^{-1}) and (b) stratiform fraction (SF in percent) for the October suppressed period. Numbers in parentheses show period means. Yellow shading denotes daylight hours.

time (Kraus 1963; Randall et al. 1991; Xu and Randall 1995).

While the precise reasons for the transition to daytime stratiform convection within the ITCZ are unclear from our analysis, the rapid adjustment of the circulation toward WTG balance in this region (Fig. 14b) suggests that the top-heavy SW CRF assists the daytime transition to a more top-heavy upward motion and Q_1 (Fig. 15). Likewise, the LW CRF in the absence of SW effects at night supports a more bottom-heavy circulation and enhanced precipitation. The link between daytime top-heavy vertical motion within the ITCZ and top-heavy shortwave heating was also found in radiative–convective equilibrium (RCE) simulations of the diurnal cycle of circulation and organized convection by Ruppert and Hohenegger (2018). Their simulations additionally suggest that both lapse-rate effects and diurnal changes in the horizontal radiative gradient are important to the nocturnal enhancement of precipitation.

5. Summary and conclusions

During the SOP of the DYNAMO field campaign, conducted over the IO from 1 October to 30 November 2011, two prominent MJO events were captured by a sounding network that consisted of one array north and one array south of the equator, referred to here as the NSA and SSA, respectively. Sites in this network took 4–8 soundings per day during this period. Using this sounding dataset along with satellite observations of winds and thermodynamic variables, an objectively analyzed gridded product was constructed. Though supplemented with ECMWF analyses to describe the larger-scale flow features over the IO basin, the gridded fields within the
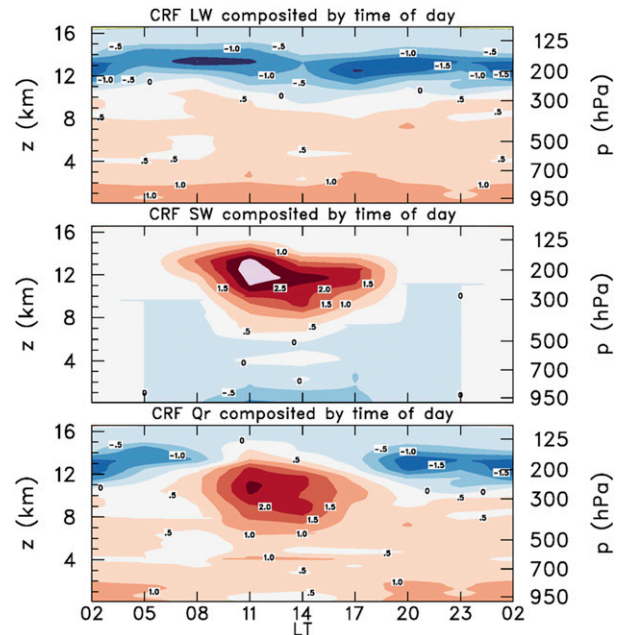

FIG. 17. Cloud radiative forcing fields (top to bottom): LW, SW, and their net (Q_r = LW + SW) composited by local time for TRMM rain rates >10 mm day^{-1} based on CombRet radiative estimates from Gan Island during DYNAMO.

sounding arrays were largely independent of any model influence. We augment this 3-h gridded product with CERES and CombRet radiative heating estimates (Feng et al. 2014) and observations of rainfall to investigate the diurnal cycle of convection during the SP of the October MJO event. While convection was suppressed over the NSA during this 14-day period, an ITCZ was present south of the equator and extended across the southern half of the SSA. Given this unique circumstance, the opportunity presents itself to examine the diurnal cycle of the ITCZ in the southern Indian Ocean (within the SSA) and its relationship to a mostly suppressed region adjacent to the ITCZ on the opposite side of the equator (the NSA), as well as determine cross-hemispheric interactions during the pre-onset phase of the MJO. The establishment of a sounding network during DYNAMO, straddling the ITCZ and with 3-hourly sonde launches, has provided the first-ever opportunity to directly observe the diurnal cycle of a local oceanic Hadley circulation.

The principal findings of this study are as follows:

- The circulation over the sounding arrays during the October SP could be characterized as a local Hadley cell embedded within a large-scale east–west upper-level divergent outflow associated with convection over Indonesia.
- Strong rising motion was present within the ITCZ region, between 5° and 8°S (i.e., over the SSA), with

compensating subsidence over the NSA and poleward of the SSA. The rising motion within the ITCZ was associated with strong low-level convergence resulting from a rapid deceleration of the southerly flow, with a portion of this flow extending beyond the ITCZ into the NSA.

- Rainfall within the ITCZ exhibited a prominent diurnal cycle with a peak-to-peak amplitude ~50% of the mean (9.7 mm day^{-1} over SSA) and a 0500 LT (2000 LT) maximum (minimum). Over the NSA, light rainfall (mean ~1 mm day^{-1}) was largely out of phase with SSA variation showing a broad morning minimum and peak rates from 1700 to 2000 LT.

- Divergent flow and vertical motion in the arrays indicate a prominent diurnal pulsing of the local Hadley cell corresponding with the diurnal cycle of the ITCZ. This diurnal pulsing is manifest in strong rising (sinking) motion over the ITCZ (NSA) in the early morning hours and a notably weaker circulation later in the day. The diurnal changes in the ITCZ circulation, while not in strict WTG balance, were consistent with a rapid adjustment toward this balance.

- Consistent with the rainfall pattern, diurnal variations in the diagnosed apparent heating Q_1 field over the SSA showed an early morning maximum with nearly twice the magnitude of the evening minimum. Apparent moistening rates over the NSA deepened vertically in the late afternoon/evening hours, reflecting a relaxed subsidence field during this time and the daytime development of the cumulus cloud field and its associated moistening effects.

- Vertical motion and Q_1 within the ITCZ exhibited a diurnal evolution from strong early morning (0500 LT) bottom-heavy (convective) profiles to weaker daytime top-heavy (stratiform) profiles. This convective transition is consistent with observations in prior studies (e.g., Houze et al. 1981; Houze 1982) and is likely assisted by enhanced SW absorption near the cloud top.

- Radiative heating in the ITCZ is characterized by top-heavy daytime shortwave warming that is likely important for suppressing deep convection during the daytime by stabilizing the column (Kraus 1963; Randall et al. 1991; Ruppert and Hohenegger 2018). Yet this warming, which is localized to the ITCZ, also promotes the daytime evolution to a top-heavy circulation, and therefore likely helps to sustain stratiform convection into the afternoon many hours after the peak in deep convection. This finding supports the notion that horizontal gradients in radiation can drive diurnal changes in circulation, as first hypothesized (albeit in a different manner) by GJ77.

- As a secondary effect of the diurnally pulsing Hadley circulation, the daytime reduction of subsidence in the

downward northern branch of the Hadley cell may have locally assisted the afternoon evolution from shallow to congestus clouds over the NSA connected with oceanic diurnal warm layers there, which have been linked to moistening of the low to midtroposphere during the pre-onset stage of the MJO (Bellenger et al. 2010; Ruppert and Johnson 2015, 2016).

While the above results are representative of the 14-day October SP, a similar but less robust Hadley cell circulation was observed (not shown) during the 11-day November SP when the ITCZ was generally south of the SSA. In the long-term TRMM rainfall record, conditions similar to the October SP with the appearance of a diurnally pulsing Hadley circulation were present 15%–20% of the time over the central IO. In addition, a recent study (Zhang and Sodowsky 2016) has shown that 55% of MJOs are initiated within 2 weeks of an ITCZ over the IO, such that the above results are likely applicable, to some degree, to the pre-onset conditions of many MJO events.

One of the objectives of this study was to utilize the high-frequency (3 h) DYNAMO observations to examine the role that different processes play in influencing the diurnal characteristics of a local Hadley circulation. Use of these observations with WTG arguments indicates that the diurnal evolution of both radiative and convective heating played an important role in controlling diurnal variations in vertical motion within the ITCZ. In contrast, over the convectively suppressed NSA, a poor correlation between observed and radiatively driven vertical motion, particularly from 1400 to 2300 LT, suggests that other processes (e.g., diurnal fluctuations in the low-level cross-equatorial flow, the influence of oceanic diurnal warm layers, and transient gravity wave activity) played a prominent role in affecting conditions within the descending branch of the local Hadley cell. While work is underway to understand the influence of these other processes, more definitive answers must await numerical simulations that can explicitly represent the higher-frequency transient aspects of the response to diabatic forcings within the Hadley circulation system (e.g., Silva Dias et al. 1987; Gonzalez et al. 2017).

REFERENCES

Albright, M. D., D. R. Mock, E. E. Recker, and R. J. Reed, 1981: A diagnostic study of the diurnal rainfall variation in the GATE B-scale area. *J. Atmos. Sci.*, **38**, 1429–1445, https://doi.org/10.1175/1520-0469(1981)038<1429:ADSOTD>2.0.CO;2.

Bain, C. L., G. Magnusdottir, P. Smyth, and H. Stern, 2010: Diurnal cycle of the intertropical convergence zone in the east Pacific. *J. Geophys. Res.*, **115**, D23116, https://doi.org/10.1029/2010JD014835.

——, J. De Paz, J. Kramer, G. Magnusdottir, P. Smyth, H. Stern, and C. C. Wang, 2011: Detecting the ITCZ in instantaneous satellite data using spatiotemporal statistical modeling: ITCZ climatology in the East Pacific. *J. Climate*, **24**, 216–230, https://doi.org/10.1175/2010JCLI3716.1.

Bellenger, H., Y. N. Takayabu, T. Ushiyama, and K. Yoneyama, 2010: Role of diurnal warm layers in the diurnal cycle of convection over the tropical Indian Ocean during MISMO. *Mon. Wea. Rev.*, **138**, 2426–2433, https://doi.org/10.1175/2010MWR3249.1.

Charney, J. G., and M. E. Stern, 1962: On the stability of internal baroclinic jets in a rotating atmosphere. *J. Atmos. Sci.*, **19**, 159–172, https://doi.org/10.1175/1520-0469(1962)019<0159:OTSOIB>2.0.CO;2.

Chen, S. S., and R. A. Houze, 1997: Diurnal variation and life-cycle of deep convective systems over the tropical Pacific warm pool. *Quart. J. Roy. Meteor. Soc.*, **123**, 357–388, https://doi.org/10.1002/qj.49712353806.

Ciesielski, P. E., W. H. Schubert, and R. H. Johnson, 2001: Diurnal variability of the marine boundary layer during ASTEX. *J. Atmos. Sci.*, **58**, 2355–2376, https://doi.org/10.1175/1520-0469(2001)058<2355:DVOTMB>2.0.CO;2.

——, and Coauthors, 2014a: Quality-controlled upper-air sounding dataset for DYNAMO/CINDY/AMIE: Development and corrections. *J. Atmos. Oceanic Technol.*, **31**, 741–764, https://doi.org/10.1175/JTECH-D-13-00165.1.

——, R. H. Johnson, K. Yoneyama, and R. K. Taft, 2014b: Mitigation of Sri Lanka island effects in Colombo sounding data and its impact on DYNAMO analyses. *J. Meteor. Soc. Japan*, **92**, 385–405, https://doi.org/10.2151/jmsj.2014-407.

——, ——, X. Jiang, Y. Zhang, and S. Xie, 2017: Relationships between radiation, clouds, and convection during DYNAMO. *J. Geophys. Res. Atmos.*, **122**, 2529–2548, https://doi.org/10.1002/2016JD025965.

Dai, A., and C. Deser, 1999: Diurnal and semidiurnal variations in global surface wind and divergence fields. *J. Geophys. Res.*, **104**, 31 109–31 125, https://doi.org/10.1029/1999JD900927.

Deser, C., and C. A. Smith, 1998: Diurnal and semidiurnal variations of the surface wind field over the tropical Pacific Ocean. *J. Climate*, **11**, 1730–1748, https://doi.org/10.1175/1520-0442(1998)011<1730:DASVOT>2.0.CO;2.

Dias, J., and O. Pauluis, 2009: Convectively coupled waves propagating along an equatorial ITCZ. *J. Atmos. Sci.*, **66**, 2237–2255, https://doi.org/10.1175/2009JAS3020.1.

Dudhia, J., 1989: Numerical study of convection observed during the Winter Monsoon Experiment using a mesoscale two-dimensional model. *J. Atmos. Sci.*, **46**, 3077–3107, https://doi.org/10.1175/1520-0469(1989)046<3077:NSOCOD>2.0.CO;2.

Duvel, J., 2015: Initiation and intensification of tropical depressions over the southern Indian Ocean: Influence of the MJO. *Mon. Wea. Rev.*, **143**, 2170–2191, https://doi.org/10.1175/MWR-D-14-00318.1.

Eliassen, A., 1983: The Charney-Stern theorem on barotropic-baroclinic instability. *Pure Appl. Geophys.*, **121**, 563–572, https://doi.org/10.1007/BF02590155.

Feng, Z., S. A. McFarlane, C. Schumacher, S. Ellis, J. M. Comstock, and N. Bharadwaj, 2014: Constructing a merged cloud-precipitation radar dataset for tropical convective clouds during the DYNAMO/AMIE experiment at Addu Atoll. *J. Atmos. Oceanic Technol.*, **31**, 1021–1042, https://doi.org/10.1175/JTECH-D-13-00132.1.

Gille, S. T., S. G. Llewellyn Smith, and S. M. Lee, 2003: Measuring the sea breeze from QuikSCAT scatterometry. *Geophys. Res. Lett.*, **30**, 1114–1117, https://doi.org/10.1029/2002GL016230.

Gonzalez, A. O., G. Mora Rojas, W. H. Schubert, and R. K. Taft, 2017: Transient aspects of the Hadley circulation forced by an idealized off-equatorial ITCZ. *J. Adv. Model. Earth Syst.*, **9**, 668–690, https://doi.org/10.1002/2016MS000837.

Gottschalck, J., P. E. Roundy, C. J. Schreck III, A. Vintzileos, and C. Zhang, 2013: Large-scale atmospheric and oceanic conditions during the 2011–12 DYNAMO field campaign. *Mon. Wea. Rev.*, **141**, 4173–4196, https://doi.org/10.1175/MWR-D-13-00022.1.

Gray, W. M., and R. W. Jacobson Jr., 1977: Diurnal variation of deep cumulus convection. *Mon. Wea. Rev.*, **105**, 1171–1188, https://doi.org/10.1175/1520-0493(1977)105<1171:DVODCC>2.0.CO;2.

Hack, J. J., W. H. Schubert, D. E. Stevens, and H.-C. Kuo, 1989: Response of the Hadley circulation to convective forcing in the ITCZ. *J. Atmos. Sci.*, **46**, 2957–2973, https://doi.org/10.1175/1520-0469(1989)046<2957:ROTHCT>2.0.CO;2.

Hendon, H. H., and K. Woodberry, 1993: The diurnal cycle of tropical convection. *J. Geophys. Res.*, **98**, 16 623–16 637, https://doi.org/10.1029/93JD00525.

Herman, M. J., and D. J. Raymond, 2014: WTG cloud modeling with spectral decomposition of heating. *J. Adv. Model. Earth Syst.*, **6**, 1121–1140, https://doi.org/10.1002/2014MS000359.

Houze, R. A., Jr., 1982: Cloud clusters and large-scale vertical motions in the tropics. *J. Meteor. Soc. Japan*, **60**, 396–410, https://doi.org/10.2151/jmsj1965.60.1_396.

——, S. G. Geotis, F. D. Marks Jr., and A. K. West, 1981: Winter monsoon convection in the vicinity of north Borneo. Part I: Structure and time variation of the clouds and precipitation. *Mon. Wea. Rev.*, **109**, 1595–1614, https://doi.org/10.1175/1520-0493(1981)109<1595:WMCITV>2.0.CO;2.

Huffman, G. J., R. F. Adler, D. T. Bolvin, G. Gu, E. J. Nelkin, K. P. Bowman, E. F. Stocker, and D. B. Wolff, 2007: The TRMM Multisatellite Precipitation Analysis: Quasi-global, multiyear, combined-sensor precipitation estimates at fine scale. *J. Hydrometeor.*, **8**, 38–55, https://doi.org/10.1175/JHM560.1.

Johnson, R. H., and G. S. Young, 1983: Heat and moisture budgets of tropical mesoscale anvil clouds. *J. Atmos. Sci.*, **40**, 2138–2147, https://doi.org/10.1175/1520-0469(1983)040<2138:HAMBOT>2.0.CO;2.

——, P. E. Ciesielski, and J. A. Cotturone, 2001: Multiscale variability of the atmospheric mixed-layer over the western Pacific warm pool. *J. Atmos. Sci.*, **58**, 2729–2750, https://doi.org/10.1175/1520-0469(2001)058<2729:MVOTAM>2.0.CO;2.

——, and ——, 2013: Structure and properties of Madden–Julian oscillations deduced from DYNAMO sounding arrays. *J. Atmos. Sci.*, **70**, 3157–3179, https://doi.org/10.1175/JAS-D-13-065.1.

——, and ——, 2017: Multiscale variability of the atmospheric boundary layer during DYNAMO. *J. Atmos. Sci.*, **74**, 4003–4021, https://doi.org/10.1175/JAS-D-17-0182.1.

——, ——, J. H. Ruppert Jr., and M. Katsumata, 2015: Sounding-based thermodynamic budgets for DYNAMO. *J. Atmos. Sci.*, **72**, 598–622, https://doi.org/10.1175/JAS-D-14-0202.1.

Kerns, B. W., and S. S. Chen, 2014: Equatorial dry air intrusion and related synoptic variability in MJO initiation during DYNAMO. *Mon. Wea. Rev.*, **142**, 1326–1343, https://doi.org/10.1175/MWR-D-13-00159.1.

Kraus, E. B., 1963: The diurnal precipitation change over the sea. *J. Atmos. Sci.*, **20**, 551–556, https://doi.org/10.1175/1520-0469(1963)020<0551:TDPCOT>2.0.CO;2.

Krishnamurti, T. N., and C. M. Kishtawal, 2000: A pronounced continental-scale diurnal mode of the Asian summer monsoon. *Mon. Wea. Rev.*, **128**, 462–473, https://doi.org/10.1175/1520-0493(2000)128<0462:APCSDM>2.0.CO;2.

Lin, J.-L., B. E. Mapes, M. Zhang, and M. Newman, 2004: Stratiform precipitation, vertical heating profiles, and the Madden–Julian oscillation. *J. Atmos. Sci.*, **61**, 296–309, https://doi.org/10.1175/1520-0469(2004)061<0296:SPVHPA>2.0.CO;2.

Madden, R. A., and P. R. Julian, 1972: Description of global-scale circulation cells in the tropics with a 40–50 day period. *J. Atmos. Sci.*, **29**, 1109–1123, https://doi.org/10.1175/1520-0469(1972)029<1109:DOGSCC>2.0.CO;2.

Magnusdottir, G., and C. C. Wang, 2008: Intertropical convergence zones during the active season in daily data. *J. Atmos. Sci.*, **65**, 2425–2436, https://doi.org/10.1175/2007JAS2518.1.

Nicholls, M. E., 2015: An investigation of how radiation may cause accelerated rates of tropical cyclogenesis and diurnal cycles of convective activity. *Atmos. Chem. Phys.*, **15**, 9003–9029, https://doi.org/10.5194/acp-15-9003-2015.

Nieto Ferreira, R., and W. H. Schubert, 1997: Barotropic aspects of ITCZ breakdown. *J. Atmos. Sci.*, **54**, 261–285, https://doi.org/10.1175/1520-0469(1997)054<0261:BAOIB>2.0.CO;2.

Nitta, T., and S. Esbensen, 1974: Heat and moisture budget analyses using BOMEX data. *Mon. Wea. Rev.*, **102**, 17–28, https://doi.org/10.1175/1520-0493(1974)102<0017:HAMBAU>2.0.CO;2.

Nuss, W. A., and D. W. Titley, 1994: Use of multiquadric interpolation for meteorological objective analysis. *Mon. Wea. Rev.*, **122**, 1611–1631, https://doi.org/10.1175/1520-0493(1994)122<1611:UOMIFM>2.0.CO;2.

Powell, S. W., R. A. Houze Jr., and S. R. Brodzik, 2016: Rainfall-type categorization of radar echoes using polar coordinate reflectivity data. *J. Atmos. Oceanic Technol.*, **33**, 523–538, https://doi.org/10.1175/JTECH-D-15-0135.1.

Randall, D. A., Harshvardhan, and D. A. Dazlich, 1991: Diurnal variability of the hydrologic cycle in a general circulation model. *J. Atmos. Sci.*, **48**, 40–62, https://doi.org/10.1175/1520-0469(1991)048<0040:DVOTHC>2.0.CO;2.

Raymond, D. J., 2000: The Hadley circulation as a radiative–convective instability. *J. Atmos. Sci.*, **57**, 1286–1297, https://doi.org/10.1175/1520-0469(2000)057<1286:THCAAR>2.0.CO;2.

Ruppert, J. H., Jr., 2016: Diurnal timescale feedbacks in the tropical cumulus regime. *J. Adv. Model. Earth Syst.*, **8**, 1483–1500, https://doi.org/10.1002/2016MS000713.

——, and R. H. Johnson, 2015: Diurnally modulated cumulus moistening in the preonset stage of the Madden–Julian oscillation during DYNAMO. *J. Atmos. Sci.*, **72**, 1622–1647, https://doi.org/10.1175/JAS-D-14-0218.1.

——, and ——, 2016: On the cumulus diurnal cycle over the tropical warm pool. *J. Adv. Model. Earth Syst.*, **8**, 669–690, https://doi.org/10.1002/2015MS000610.

Ruppert, J. H., Jr., and C. Hohenegger, 2018: Diurnal circulation adjustment and organized deep convection. *J. Climate*, https://doi.org/10.1175/JCLI-D-17-0693.1, in press.

Sakaeda, N., G. Kiladis, and J. Dias, 2017: The diurnal cycle of tropical cloudiness and rainfall associated with the Madden–Julian oscillation. *J. Climate*, **30**, 3999–4020, https://doi.org/10.1175/JCLI-D-16-0788.1.

Schubert, W. H., P. E. Ciesielski, D. E. Stevens, and H.-C. Kuo, 1991: Potential vorticity modeling of the ITCZ and the Hadley circulation. *J. Atmos. Sci.*, **48**, 1493–1509, https://doi.org/10.1175/1520-0469(1991)048<1493:PVMOTI>2.0.CO;2.

——, ——, C. Lu, and R. H. Johnson, 1995: Dynamical adjustment of the trade wind inversion layer. *J. Atmos. Sci.*, **52**, 2941–2952, https://doi.org/10.1175/1520-0469(1995)052<2941:DAOTTW>2.0.CO;2.

Silva Dias, P. L., J. P. Bonatti, and V. E. Kousky, 1987: Diurnally forced tropical tropospheric circulation over South America. *Mon. Wea. Rev.*, **115**, 1465–1478, https://doi.org/10.1175/1520-0493(1987)115<1465:DFTTCO>2.0.CO;2.

Sobel, A. H., J. Nilsson, and L. M. Polvani, 2001: The weak temperature gradient approximation and balanced tropical moisture waves. *J. Atmos. Sci.*, **58**, 3650–3665, https://doi.org/10.1175/1520-0469(2001)058<3650:TWTGAA>2.0.CO;2.

Sodowsky, R., 2016: Cloud and rainfall statistics from the MJO and the ITCZ over the Indian Ocean. *32nd Conf. on Hurricanes and Tropical Meteorology*, San Juan, PR, Amer. Meteor. Soc., 9B.5, https://ams.confex.com/ams/32Hurr/webprogram/Paper293247.html.

Stevens, D. E., and P. E. Ciesielski, 1986: Inertial instability of horizontally sheared flow away from the equator. *J. Atmos. Sci.*, **43**, 2845–2856, https://doi.org/10.1175/1520-0469(1986)043<2845:IIOHSF>2.0.CO;2.

Sui, C. H., K. M. Lau, Y. N. Takayabu, and D. A. Short, 1997: Diurnal variations in tropical oceanic cumulus convection during TOGA COARE. *J. Atmos. Sci.*, **54**, 639–655, https://doi.org/10.1175/1520-0469(1997)054<0639:DVITOC>2.0.CO;2.

Tao, W. K., S. Lang, J. Simpson, C.-H. Sui, B. Ferrier, and M. D. Chou, 1996: Mechanisms of cloud–radiation interaction in the tropics and midlatitudes. *J. Atmos. Sci.*, **53**, 2624–2651, https://doi.org/10.1175/1520-0469(1996)053<2624:MOCRII>2.0.CO;2.

Waliser, D. E., and C. Gautier, 1993: A satellite-derived climatology of the ITCZ. *J. Climate*, **6**, 2162–2174, https://doi.org/10.1175/1520-0442(1993)006<2162:ASDCOT>2.0.CO;2.

Wang, C.-C., and G. Magnusdottir, 2005: ITCZ breakdown in three-dimensional flows. *J. Atmos. Sci.*, **62**, 1497–1512, https://doi.org/10.1175/JAS3409.1.

Wheeler, M. C., and H. H. Hendon, 2004: An all-season real-time multivariate MJO index: Development of an index for monitoring and prediction. *Mon. Wea. Rev.*, **132**, 1917–1932, https://doi.org/10.1175/1520-0493(2004)132<1917:AARMMI>2.0.CO;2.

Wielicki, B. A., B. R. Barkstrom, E. F. Harrison, R. B. Lee III, G. L. Smith, and J. E. Cooper, 1996: Clouds and the Earth's Radiant Energy System (CERES): An Earth Observing System experiment. *Bull. Amer. Meteor. Soc.*, **77**, 853–868, https://doi.org/10.1175/1520-0477(1996)077<0853:CATERE>2.0.CO;2.

Woolnough, S. J., J. M. Slingo, and B. J. Hoskins, 2004: The diurnal cycle of convection and atmospheric tides in an aquaplanet GCM. *J. Atmos. Sci.*, **61**, 2559–2573, https://doi.org/10.1175/JAS3290.1.

Xu, K.-M., and D. A. Randall, 1995: Impact of interactive radiative transfer on the macroscopic behavior of cumulus ensembles. Part II: Mechanisms for cloud-radiation interaction. *J. Atmos. Sci.*, **52**, 800–817, https://doi.org/10.1175/1520-0469(1995)052<0800:IOIRTO>2.0.CO;2.

Xu, W., and S. A. Rutledge, 2014: Convective characteristics of the Madden–Julian oscillation over the central Indian Ocean observed by shipborne radar during DYNAMO. *J. Atmos. Sci.*, **71**, 2859–2877, https://doi.org/10.1175/JAS-D-13-0372.1.

——, and ——, 2016: Time scales of shallow-to-deep convective transition associated with the onset of the Madden–Julian oscillation. *Geophys. Res. Lett.*, **43**, 2880–2888, https://doi.org/10.1002/2016GL068269.

——, ——, C. Schumacher, and M. Katsumata, 2015: Evolution, properties, and spatial variability of MJO convection near and off the equator during DYNAMO. *J. Atmos. Sci.*, **72**, 4126–4147, https://doi.org/10.1175/JAS-D-15-0032.1.

Yanai, M., S. Esbensen, and J.-H. Chu, 1973: Determination of bulk properties of tropical cloud clusters from large-scale heat and moisture budgets. *J. Atmos. Sci.*, **30**, 611–627, https://doi.org/10.1175/1520-0469(1973)030<0611:DOBPOT>2.0.CO;2.

Yoneyama, K., C. Zhang, and C. N. Long, 2013: Tracking pulses of the Madden–Julian. *Bull. Amer. Meteor. Soc.*, **94**, 1871–1891, https://doi.org/10.1175/BAMS-D-12-00157.1.

Zhang, C., 2013: The Madden–Julian oscillation: Bridging weather and climate. *Bull. Amer. Meteor. Soc.*, **94**, 1849–1870, https://doi.org/10.1175/BAMS-D-12-00026.1.

——, and R. C. Sodowsky, 2016: Large-scale and convective characteristics of the ITCZ and MJO initiation over the Indian Ocean. *2016 Fall Meeting*, San Francisco, CA, Amer. Geophys. Union, Abstract A31H-0149.

——, M. McGauley, and N. A. Bond, 2004: Shallow meridional circulations in the tropical Eastern Pacific. *J. Climate*, **17**, 133–139, https://doi.org/10.1175/1520-0442(2004)017<0133:SMCITT>2.0.CO;2.

——, D. S. Nolan, C. D. Thorncroft, and H. Nguyen, 2008: Shallow meridional circulations in the tropical atmosphere. *J. Climate*, **21**, 3453–3470, https://doi.org/10.1175/2007JCLI1870.1.

——, J. Gottschalck, E. D. Maloney, M. W. Moncrieff, F. Vitart, D. E. Waliser, B. Wang, and M. C. Wheeler, 2013: Cracking the MJO nut. *Geophys. Res. Lett.*, **40**, 1223–1230, https://doi.org/10.1002/grl.50244.